Withdrawn NIST Technical Series Publication

Warning Notice

The attached publication has been withdrawn (archived), and is provided solely for historical purposes. It may have been superseded by another publication (indicated below).

Withdrawn Publication	
Series/Number	NIST TN 2327
Title	The Burning Characteristics of 3 m to 6 m Dry Douglas-Fir Trees
Publication Date(s)	February 05,2025
Withdrawal Date	May 01,2025
Withdrawal Note	Superseded by updated version

Superseding Publication(s) *(if applicable)*

The attached publication has been **superseded by** the following publication(s):

Series/Number	NIST TN 2327r1
Title	The Burning Characteristics of 3 m to 6 m Dry Douglas-Fir Trees
Author(s)	Erik Johnsson; Giovanni Di Cristina; Eric Mueller; Matthew Bundy; Tony Chakalis; Marco Fernandez; Anthony Hamins.
Publication Date(s)	May 01,2025
URL/DOI	https://doi.org/10.6028/NIST.TN.2327r1

Additional Information *(if applicable)*

Contact	
Latest revision of the attached publication	
Related Information	
Withdrawal Announcement Link	

NATIONAL INSTITUTE OF STANDARDS AND TECHNOLOGY
U.S. DEPARTMENT OF COMMERCE

Date Updated: May 1, 2025

NIST Technical Note
NIST TN 2327

The Burning Characteristics of 3 m to 6 m Dry Douglas-Fir Trees

Erik Johnsson
Giovanni Di Cristina
Eric Mueller
Matthew Bundy
Tony Chakalis
Marco Fernandez
Anthony Hamins

This publication is available free of charge from:
https://doi.org/10.6028/NIST.TN.2327

NATIONAL INSTITUTE OF STANDARDS AND TECHNOLOGY
U.S. DEPARTMENT OF COMMERCE

NIST Technical Note
NIST TN 2327

The Burning Characteristics of 3 m to 6 m Dry Douglas-Fir Trees

Erik Johnsson
Giovanni Di Cristina
Eric Mueller
Matthew Bundy
Tony Chakalis
Marco Fernandez
Anthony Hamins
Fire Research Division
Engineering Laboratory

This publication is available free of charge from:
https://doi.org/10.6028/NIST.TN.2327

February 2025

U.S. Department of Commerce
Jeremy Pelter, Acting Secretary of Commerce

National Institute of Standards and Technology
Craig Burkhardt, Acting Under Secretary of Commerce for Standards and Technology and Acting NIST Directory

NIST TN 2327
February 2025

NIST Technical Series Policies

Publication History
Approved by the NIST Editorial Review Board on 2024-01-16

How to Cite this NIST Technical Series Publication
Johnsson E, Di Cristina G, Mueller E, Bundy M, Chakalis T, Fernandez M, Hamins A (2025) The Burning Characteristics of 3 m to 6 m Dry Douglas-Fir Trees. (National Institute of Standards and Technology, Gaithersburg, MD), NIST Technical Note (TN) NIST TN 2327. https://doi.org/10.6028/NIST.TN.2327

Author ORCID iDs
Matthew Bundy: 0000-0002-1138-0307
Giovanni Di Cristina Torres: 0000-0002-0799-3418
Anthony Chakalis: 0009-0004-4331-7101
Marco Fernandez: 0000-0002-4227-8866
Anthony Hamins: 0000-0001-7531-4256
Rik Johnsson: 0000-0003-1170-7370
Eric Muller: 0000-0002-0838-6820

Contact Information:
anthony.hamins@nist.gov

Abstract

A series of experiments is reported on the burning behavior of dry, 3 m to 6 m tall, Douglas-fir trees. The preconditioning and ignition of the trees using a natural gas ring-type burner was intended to provide data for characterization and modeling of outdoor wildland-urban interface (WUI) fire hazards. The measurements were conducted in the open under quasi-quiescent conditions. The measurements reported here include the transient, peak, and total heat release rates, the yields of carbon monoxide (CO) and soot, the mass loss, and the near and far-field heat fluxes. The appearance of the trees was captured by photogrammetry. The fires were documented by video cameras from several perspectives. Measurements of the heat flux to the surroundings from the specimens were used to estimate the radiative fraction of the fires.

The total heat release measured by oxygen consumption calorimetry and the ideal heat release calculated from the product of the total mass loss and the heat of combustion were found to be in reasonable agreement. The ratio of the CO yield to the soot yield was nearly constant over a wide range of total heat release rates. A preliminary rescaling methodology is introduced to adjust the transient heat release rate, accounting for the calorimeter system's time response. The results provide unique calorimetric data which can be useful for development of design fire scenarios. The data from the study are available on the NIST Fire Calorimetry Database (FCD).

Keywords

burning rate; calorimetry time response; fire calorimetry database; trees; heat release rate; radiative emission

Table of Contents

List of Figures

List of Tables

Acknowledgments

The authors are grateful to Phillip Deardorff, Justin Mills, and Artur Chernovsky of NIST for their outstanding technical support during the test series.

1. Introduction

A series of fire experiments is reported that investigates the burning characteristics of large trees under quasi-quiescent conditions. The objective of this study is to expand the NIST Fire Calorimetry Database (FCD) through measurements of the character of the fires with an emphasis on the transient heat release rate. The FCD contains hundreds of measurement results of fire experiments conducted since 2017 at NIST's National Fire Research Laboratory (NFRL). The FCD is used by fire protection engineers to support engineering analysis including performance-based design, as well as by fire safety science researchers interested in information about the burning of specific types of items. The specimens contained in the database include single burning items, fully furnished rooms, controlled burners, well-characterized fuels, and composite fuels typically of unknown composition. A focus of the FCD is the accuracy of the transient heat release rate (HRR) measurement and its uncertainty. A description of the instrumentation for each of the FCD measurements is provided in Bryant and Bundy [2019]. The FCD includes a summary of the measurement results, their uncertainty, and the experimental conditions. The following is a list of the measurement results typically provided in the FCD (not all values are provided for every test):

- a brief description of the test specimen
- transient HRR [kW]
- peak HRR [kW]
- time to peak HRR [s]
- total heat released [MJ]
- quality confirmation of the HRR
- initial specimen mass [kg of dry fuel]
- mass change of the specimen [kg of dry fuel]
- net effective heat of combustion the ratio of the total heat release to the change in specimen mass) [MJ/(kg of dry fuel)]
- O_2 consumed per change in specimen mass [(kg O_2 consumed)/(kg of dry fuel)]
- CO_2 yield [(kg of CO_2)/(kg of dry fuel)]
- CO yield [(kg of CO)/(kg of dry fuel)]
- soot yield [(kg of soot)/(kg of dry fuel)]
- test duration (s)

For this series of tests, the FCD provides the dry specimen mass, that is, a correction is applied for the water content of the fuel mass. The FCD also provides a list of input parameters and conditions characterizing the experiments, which includes the following items:

- Baseline exhaust flow [kg/s]
- Exhaust hood size [m]
- Effective exhaust duct diameter [m]

- Exhaust flow correction factor [-]
- Net heat of combustion (per unit mass of O_2) [kJ/g]
- Net heat of combustion (per unit mass fuel) [kJ/g]
- Exhaust hood size [m^2]

The specimens selected for characterization in this study were Douglas-fir trees. Douglas-fir is an evergreen conifer species (*Pseudotsuga menziesii*) and a member of the pine family that contains soft, flat needles roughly 1 cm to 4 cm in length. It was selected for study as it is a common tree species in the Western United States and easily obtainable throughout the year.

The burning rate of a tree fire is influenced by many physical, geometric, and ignition scenario attributes. These include a specimen's dryness, dimensions, configuration, the environmental conditions (humidity, temperature, wind, etc.), and the strength and location of the ignition source, among other parameters. It is impossible to provide test results for every conceivable permutation of these parameters. Nevertheless, the heat release rates reported in this study can be useful in guiding engineering analysis and for providing a reference for validation and application of fire models.

This main body of this report is broken into five sections. The remainder of this introduction presents a brief review of previous studies on tree fires. 2 describes the experimental methods including the ignition scenarios and describes the test specimens. Section 3 presents an overview of the experimental results including an estimate of the radiative fraction. Section 4 summarizes the results and findings. Section 5 presents the references cited in this report. Six appendices accompany this report. Appendix A contains photos with overlaid dimensions and a description of each of the specimens. Appendix B presents the transient calorimetry data. Appendix C lists the transient mass loss. Appendix D presents the near-and far-field transient heat flux measurements. discusses uncertainty in the photogrammetry measurements. Appendix E discusses correction of the time response of the transient heat release rate measurements. Appendix F discusses the uncertainty in the photogrammetry method.

As described in the next subsection, there have been many previous studies on the burning of vegetation and some studies on the burning of Douglas-fir trees. The experiments conducted in this study complement previous research, providing comprehensive calorimetric information with reported uncertainty as well as a full video record of large tree fires burning under fully ventilated quasi-quiescent conditions.

1.1. Previous Work

A significant amount of work has been conducted on tree burning. Mell et al. [2009] measured the mass loss and local heat flux to targets 2 m and 3 m away from the center of 2 m and 5 m tall Douglas-fir trees. The study investigated how various factors, such as moisture content and tree size, affect the burning rate and heat flux. Completeness of the burning of Douglas-fir differed according to three ranges of moisture content (MC) on a dry basis: MC < 30 %, 30 % < MC < 70 %, and MC > 70 % with the lowest moisture content trees burning well and the high moisture content trees not burning at all. The results revealed that higher moisture levels significantly reduced the fire heat release rate, underscoring the importance of moisture content in wildfire management. The importance of moisture content is considered in many other studies. Schneider et al. [2020] tested the possibility of fire spread by radiation from adjacent burning trees. Three trees spaced 20 cm to 30 cm apart from the nearest branches of the target tree and positioned around the target tree were simultaneously ignited using gas burners. Only about half of the experiments led to ignition of the target tree. Measurements of the mass loss rates and local heat fluxes found that the target tree's moisture content affected the propensity for its ignition.

The importance of moisture content has also been the focus of experiments investigating the heat release rate of dry "Christmas" trees, which have shown that keeping a tree watered reduces fire risk [Bigda 2021; Hoehler 2020]. Accary et al. [2024] conducted five experiments measuring the mass burning rate of very dry (6% ≤ moisture content ≤ 9%), 2 m tall, (single) Douglas-fir trees burning in the open under fully-ventilated conditions. The trees were ignited using a 0.8 m circular methane gas burner placed 30 cm below the tree base. The near-field heat flux and centerline temperature measurements were compared to simulations using four commonly used computational fluid dynamics fire models. The experiments and simulations showed that the HRR profile is very sensitive to the ignition protocol. Accary [2024] concludes that the ignition event must be well-controlled to ensure experimental repeatability.

Babrauskas [2001] conducted an extensive number of fire experiments investigating the HRR of single 2 m tall Douglas-fir trees that were placed in a watering stand. Various watering programs were used such that the tree moisture content on a dry basis varied from about 3 % to 160 %. The trees were positioned in a room corner configuration for fire testing. The ratio of the measured peak HRRs to the dry mass of the trees was found to be roughly proportional to the reciprocal of the foliar moisture content. The same correlation held for various species of burning shrubs burning under well-ventilated conditions. Babrauskas [2016] concludes that the main variables affecting the HRR of "Christmas" trees are the moisture content of the needles, the mass of the tree, the species type, and the ignition source used.

Modarres et al. [2024] burned a series of single, small, Eucalyptus trees of different ages, varying between 6 months and 5 years. The moisture content ranged between 74 % and 152 % and varied with age and tree component (e.g. foliage versus branches). The trees were burned by igniting trays of alcohol at their base. Measurements included the mass loss rate, the centerline plume temperatures, and heat flux to a nearby target. Older trees were found to burn for a shorter duration with a higher peak mass loss rate and higher peak heat flux, which was attributed to their lower relative moisture content.

Sung et al. [2024] recently conducted a series of experiments on some vegetative fuels including single, 0.9 m to 1.8 m tall, Douglas-fir trees. The measurements mirror many of the measurements conducted in this study and the results complement the results presented here for smaller trees. Few other studies have measured the soot and carbon monoxide (CO) yields from burning trees and none found in our literature review have reported on the far-field heat flux[1] and the radiative fraction of the fire. In addition, except for Mell et al. [2009], all previous studies were limited to a tree height of nominally 2 m or less.

[1] Far-field refers to distances sufficiently far from the source such that a single location radiative flux measurement allows estimation of the radiative fraction of a fire.

2. Experimental Apparatus and Procedure

The experiments investigated 6 large (approximately 3 m to 6 m tall) Douglas-fir trees in the open under quasi-quiescent conditions (without an applied wind field). The experiments were conducted under the 20 MW exhaust hood calorimeter at NIST's National Fire Research Laboratory (NFRL). A schematic of the hood and laboratory space is shown in Fig. 1. The subsections below elaborate further on the hood and describe the setup, instrumentation, and details of the experimental series.

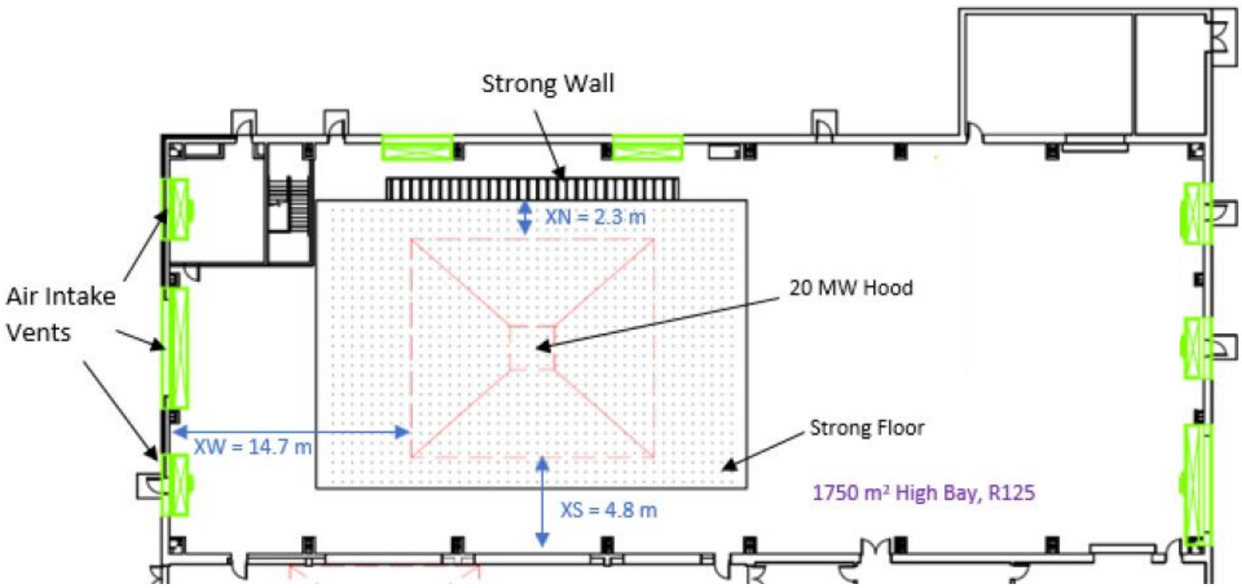

Figure 1. Floor plan of the National Fire Research Laboratory's Room 125, housing the 20 MW exhaust hood.

2.1. Experimental Setup

The 6 large trees were burned one at a time under a 20 MW capacity calorimeter with a 13.8 m × 15.4 m canopy hood. The 20 MW exhaust hood captured the fire effluent for quantification of the heat release as a function of time. A large round exhaust duct (2.4 m diameter) was located 15.3 m above the floor.

Figure 2 shows a plan view of the experimental setup under the 13.8 m × 15.4 m canopy hood. The instrumentation and attachment I-beam columns are shown in their relative positions. The test specimen was placed directly below the center of the exhaust duct. The exhaust flow used during the experiments was approximately 70 kg/s and is listed in the FCD. Side skirts located 6.1 m above the floor were suspended from and surrounded the exhaust hood. Multiple heat flux gauges and plate thermometers were arranged vertically at designated locations as described in detail in Section 2.3.4.

The trees were ignited using a hexagonal-shaped, natural gas burner at the base of the tree (see Section 2.5.1). The trees were allowed to burn until flames and smoldering self-extinguished.

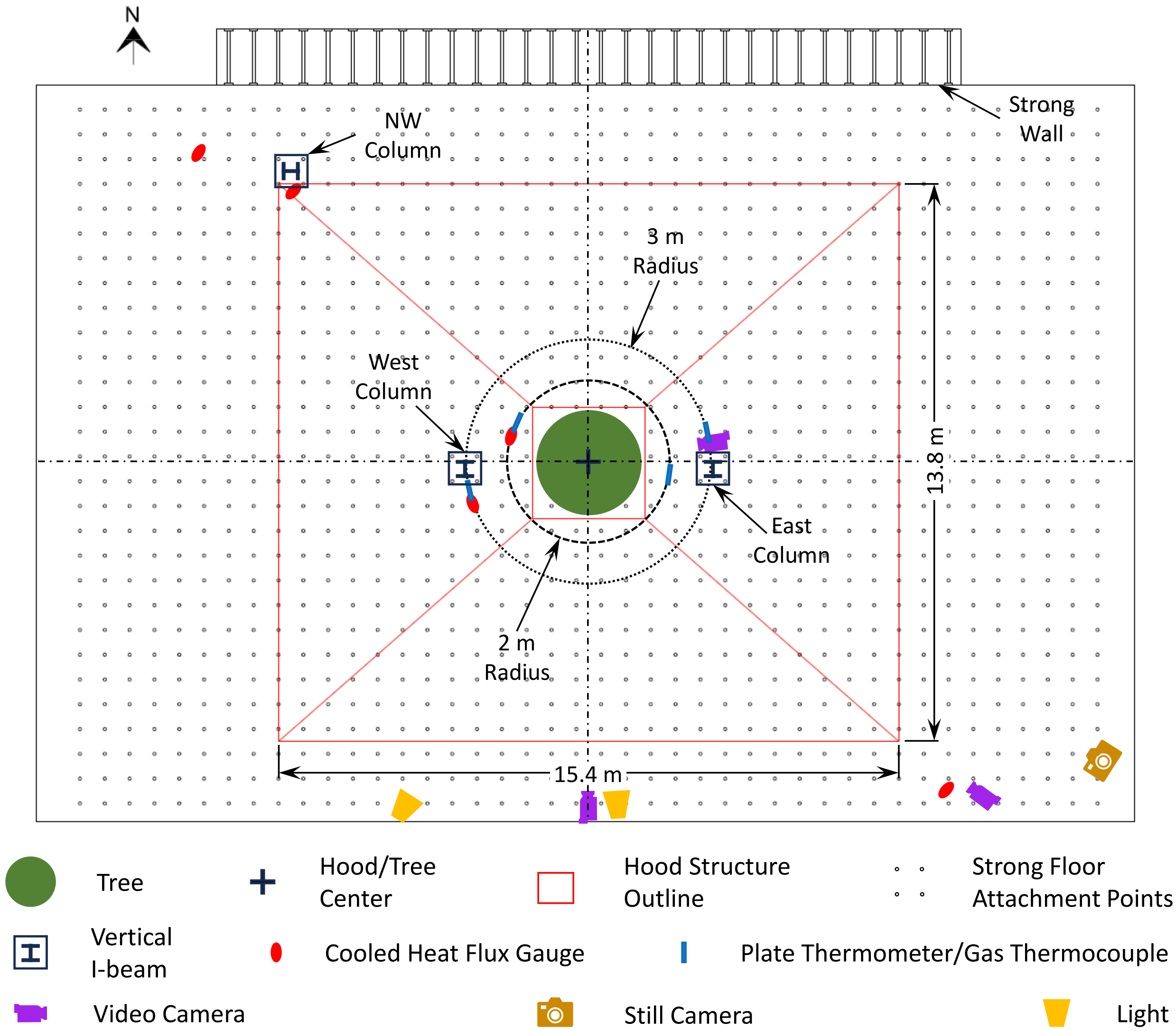

Figure 2. A scale plan view drawing of the area under the 13.8 m × 15.4 m canopy hood showing instrumentation locations.

2.2. Specimens

Table 1 lists the details of each tree used in this study, including dimensions, mass, and moisture content (MC). Three pairs of trees were selected for study based on their height, which was roughly 4 m (Trees 1 and 2), 4.5 m (Trees 3 and 4), and 6 m (Trees 5 and 6). Although there was natural variation among each pair, Table 1 shows each pair also had similar widths, masses, and moisture content.

The trees' heights and widths were measured using photogrammetry; photographs to create three-dimensional (3D) models. Photos of each of the specimens overlaid with their dimensions are listed by test number in Appendix A. The trees were stored indoors under ambient conditions for about 2 months at an average temperature was 25.0 °C ± 1.4 °C and the relative humidity varied between 41 % to 83 % with an average value of 62 % ± 10 %. The moisture content of the trees was monitored daily and the final dry basis moisture content is reported in Table 1.

The tree trunks were secured to the base of the stands, which were positioned about 0.35 m above the floor. The widths listed are maximum extent rather than an average and are only as viewed from the south side. The combined expanded uncertainty of the initial (dry) tree masses (corrected for water content) with a 95 % confidence level are listed in Table 1 based on measurement resolution, repeat measurements, calibration with standard weights, and manufacturer information about the weighing system. The expanded (k=2) uncertainty of the heights and widths was estimated to be ±3.0 cm.

Table 1. Characterization of the specimens including the trees' height and maximum width[a] using photogrammetry,[b] the initial tree mass corrected for moisture content (MC), and the measured dry basis MC percentage.

Test #	Height from Floor (m)	Height from Stand (m)	Width (m)	Initial Dry Mass (kg)	MC (%)
1	3.74	3.39	2.35	14.30 ± 0.57	7.8 ± 1.9
2	4.03	3.68	2.09	18.47 ± 0.57	7.8 ± 1.9
3	4.61	4.26	2.67	27.46 ± 0.57	8.6 ± 2.0
4	4.46	4.10	2.51	24.28 ± 0.57	8.4 ± 2.0
5	6.14	5.79	2.71	54.27 ± 0.57	11.0 ± 2.6
6	6.18	5.83	3.05	48.64 ± 0.57	13.0 ± 3.1

a. The combined expanded uncertainties of the height and width are equal to ±3.0 cm.
b. See Appendix A for photos of the specimens and Section 2.3.7 for a discussion of the photogrammetry.

Figure 3 shows the diameters of the tree trunks measured post-fire with calipers as a function of distance above the tree stand base (the surface the trunk rested on). These measurements are considered representative of the unburned trunk diameter as post-fire inspection showed only a shallow char layer. The six tree specimens were of various sizes with their height varying from 3 m to 6 m. The trunk diameters at the base of the trees ranged from about 11 cm to 17 cm. The change in trunk diameter with distance above the tree stands in Figure 3 was approximately linear with the slopes varying from roughly -0.004 (cm/cm) to -0.003 (cm/cm).

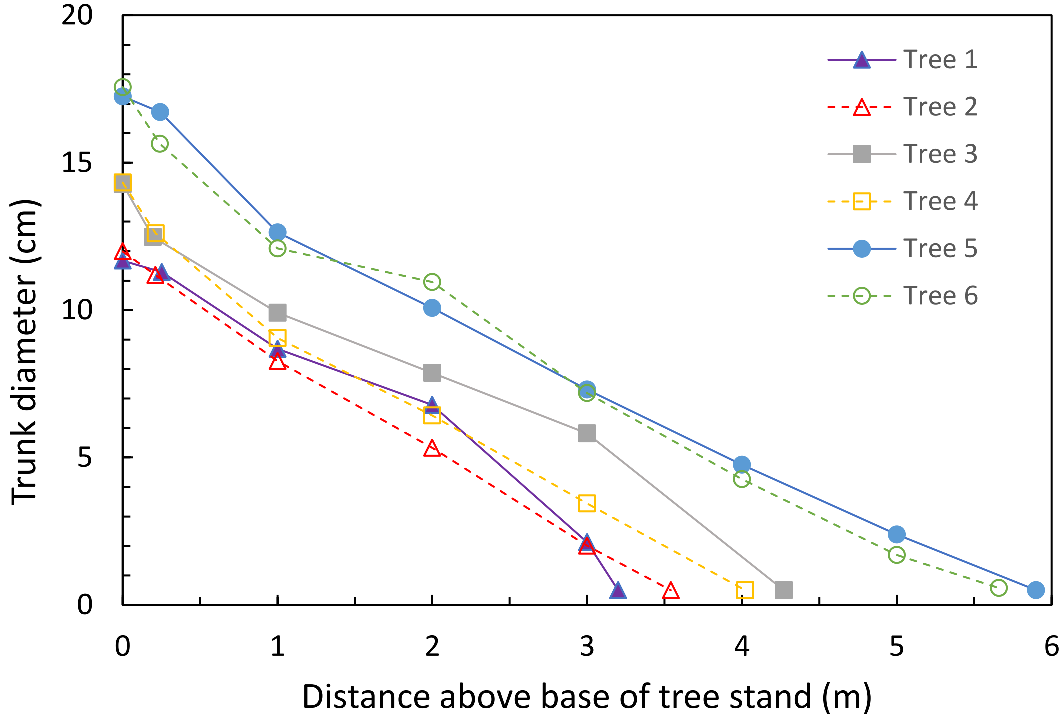

Figure 3. Post-fire trunk diameter versus distance above the tree stand for the six Douglas-fir specimens with measurement uncertainty of ±1 cm.

2.3. Instrumentation

Several measurements were made in this study in addition to calorimetry and items normally reported as part of the FCD (see Section 1), including:

- Moisture content of the trees using a moisture analyzer
- Transient mass loss using a load cell system
- Transient radiative heat flux to targets using cooled heat flux gauges and plate thermometers
- Video camera recordings from several perspectives

The data were sampled at 1 kHz with the averages over each second recorded at 1 Hz. A description of each of these measurements is given below.

2.3.1. Calorimetry

Information about the calorimeters, including a detailed discussion of the NIST oxygen consumption calorimetry measurement method, measurement uncertainty, and validation have been documented [Bryant, 2019]. A fuel consumption calorimetry system (natural gas burners and flow control) used to generate precise amounts of heat release was used to provide a rigorous evaluation of the oxygen consumption calorimetry system and its uncertainty. The expanded (k=2) combined uncertainty of the calorimetry system was found to range between 5.6 % and 11.3 %, depending on the experimental conditions [Bryant, 2019]. In this study, the heat of combustion of Douglas-fir and its uncertainty is taken from the literature as described in Section 3.2 below. The time response of the 20 MW calorimetry system has a time constant of approximately 8 s based on analysis of imposed square-wave changes to the HRR determined from calibration experiments using pulses of a natural gas fire imposed in a near square wave shape for various durations. These results suggest that it can accurately resolve fire events lasting more than 20 s to better than 92 % of the actual peak value.

2.3.2. Moisture Content

The moisture content of the trees was measured before each test. It was observed that the needles were not uniform in appearance nor moisture content, with needles towards the branch tips featuring higher moisture content, green appearance, and more pliable than needles closer to the tree trunk. The details of the distribution appeared to differ from branch to branch. For this reason, the moisture content of the tree was characterized by taking spatially distributed samples and combining them to achieve an average measurement. One gram to three gram samples of needles and stems were collected the day of the test from various locations in the tree. Samples of approximately the same mass were collected from four sides of the tree, combined, and saved in a sealed plastic bag for storage until testing. A comparison of samples collected high and low in these dry trees yielded similar results. On the day of testing, samples were collected and loaded into a moisture analyzer for measurement of the moisture content. Several core samples low on the trunk were also taken for moisture analysis before and after the experiments.

The moisture analyzer was programmed to run at a temperature of 110°C with the criteria to end the moisture analysis defined as a mass rate of change of the sample less than 0.02 %/min. This temperature was selected to remove all water while preventing the removal of volatile compounds. The termination criteria were conservative, and tests with a smaller rate of change termination criteria showed no discernable difference for tests using the same sample batch.

The calibration of the moisture analyzer was evaluated and found to be better than 2 % based on comparison experiments using an oven (at the same oven temperatures of 110 °C) and a precision scale (Siemens Model #K1000) for the same sample foliage batch. Measurements using the analyzer showed a high level of repeatability (better than 2 %) for the same sample batch. The standard deviation increased to 12 % when different sample batches were tested from the same tree using the same collection method, presumably due to natural variation.

The analyzer outputs the moisture content on a wet basis percentage (MC_{wet}). Measurements were then converted to a dry basis percentage using the following equation:

$$MC = 100\ MC_{wet}/(100 - \ MC_{wet}) \tag{1}$$

Table 1 lists the mean dry basis moisture content value for each of the trees along with its combined expanded uncertainty.

2.3.3. Mass Loss

The transient mass loss was determined using an Intercomp (model CW250) system of four load cells. The capacity of each module was 200 kg with a resolution of 0.2 kg. The four load cells were placed under the corners of the rectangular load cell platform upon which the tree stand and the tree itself were placed. Before and after each experiment, the mass of the load cell platform, tree stand and supports, and any other objects on the platform were measured so they could be subtracted from the total mass to obtain the initial and final tree masses.

2.3.4. Heat Flux to Targets

The transient heat flux to targets was measured using water-cooled heat flux gauges and plate thermometers in the near- and far-field. The near-field measurements were designed to follow the measurements of Mell et al. [2009].

2.3.4.1. Heat Flux Gauges

Table 2 lists the ten water-cooled, wide-view angle (180°), thermopile-type, total heat flux sensors that were directed towards the central axis of each tree. Three cooled gauges were located at a 2 m radial distance from the tree axis on the western side of the tree at 3 heights from the mounting surface of the tree stand (i.e., the base of the tree trunk): 0.2 m, 2.3 m, and 4.5 m. The same arrangement of an additional three cooled gauges was located at a 3 m radial distance, also on the western side of the tree, but arranged so their view of the tree was not blocked by the 2 m radius array. Two more cooled gauges were located at a 10 m radius northwest of the tree at 2.3 m and 6.0 m heights. Finally, two additional cooled gauges were positioned 2.3 m high at 12 m radii, one northwest of the tree (arranged to not be blocked by the 10 m gauges) and the other southwest of the tree. The locations of the gauges relative to the tree are shown in Figure 2. The gauges positioned at 12 m could not be much further from the trees to avoid shadowing of flames by the exhaust hood skirts.

Huskeflux model SBG01 and Medtherm 64 Series heat flux gauges were used to measure the incident heat flux. The gauges were calibrated using a secondary standard gauge in a well-characterized facility [Pitts, 2006]. The heat flux background signal, which increased during the burning period as the fire heated the surroundings, was subtracted from the signal. Its uncertainty was estimated as 3 %. The combined (k=2, expanded) uncertainty for the heat flux measurement is estimated as 11 %.

The locations and gauge types are listed in Table 2. The heights, Z, listed in the table are relative to the tree stand. The distance from the base of the tree trunk to the floor was 35.4 cm. The radius, R, was measured relative to the load cell platform or tree center, and the angle, theta, was measured relative to north which was a line passing through the center and perpendicular to the strong wall shown at the top of Figure 2. The last column in Table 2 provides the data label for each sensor.

Table 2. Water-cooled heat flux gauge locations and descriptions.

Direction Relative to Tree	Distance, R (m)	Height, Z (m)	Theta (°)	Gauge Type	Gauge Range (kW/m^2)
West	1.99	0.2	272.2	Medtherm	200
West	1.99	2.3	272.2	Medtherm	200
West	1.99	4.5	272.2	Medtherm	200
West	2.99	0.2	253.9	Huskeflux	100
West	2.99	2.3	253.9	Huskeflux	100
West	2.99	4.5	253.9	Huskeflux	100
Northwest	9.98	2.3	312.4	Huskeflux	5
Northwest	9.98	6.0	312.4	Huskeflux	5
Northwest	12.12	2.3	308.4	Huskeflux	5
Southwest	11.96	2.3	132.5	Huskeflux	5

An estimate of the total radiative energy (TRE_i) was determined from the measurements at the two far-field heat flux gauges by integrating the measured radiative heat flux over the burning period (from ignition to the end of the experiment, t_e) at each of the measurement locations:

$$TRE_i = \int_0^{t_e} 4\pi \, R_i^2 \, \dot{q}_i^{"} \, dt \qquad (2)$$

where ($\dot{q}_i^{"}$) is the radiative heat flux measured at a distance (R_i) from the fire at the i^{th} gauge. The far-field gauge results may differ due to shadowing created by unburnt portion of the trees, which may be particularly evident for non-symmetric ignitions. Nevertheless, the average of the measured fluxes can be considered representative of the radiative emission from the fire. For suitably far distances from the fire, the ratio of the average total radiated energy to the surroundings ($\overline{TRE_i}$) to the total heat release rate can be used to estimate the average radiative fraction (χ_{rad}) over the entire duration of the fire:

$$\chi_{rad} = \frac{\overline{TRE_i}}{\Delta m \, H_c} \cong \frac{\overline{TRE_i}}{THR} \qquad (3)$$

where Δm is the total mass loss, that is, the difference between the initial and final fuel mass, H_c is the net heat of combustion per unit mass of fuel assuming water as a gaseous product, and THR is the total integrated heat release measured by calorimetry. The value of χ_{rad} represents the radiative fraction over the entire burning period, not just the flaming period. Analysis shows that using the THR value rather than the product of Δm and H_c in the denominator of Eq. (3) reduces the relative uncertainty of $\chi_{rad.}$ Using THR in the equation assumes that the combustion efficiency is unity, which is not unreasonable for these fires which were not very smoky and had bluish streaks[2] on the edge of the luminous flame plume and relatively small soot yields as discussed in Section 3.4.1. The combined expanded (k = 2) uncertainty of χ_{rad} is estimated as 17 % based on the uncertainties of TRE and THR.

2.3.4.2. Plate Thermometers

Plate thermometers (PT) are robust sensors that can survive in hostile environments, and they were chosen for this series as additional heat flux measurements primarily due to their low cost and lack of need for cooling water. The PT design was taken from the literature (Wickstrom, 1994) was modified for faster response and simpler manufacture as described in detail in Putorti [2015]. A PT consisted of 0.51 mm diameter (24 AWG) Type-K thermocouple wires welded to the back side of a 100 mm by 100 mm Inconel® 600 plate (the front side faces the heat source). The plate is backed by a 25.4 mm thick insulation (ceramic fiber blanket) layer. Metal strips on the back side of the insulation are used to hold it together with the front plate using screws and washers.

[2] The bluish streaks that were observed are not visible in the over-exposed videos on the FCD and are generally challenging to record by video.

A photo of one of the modified PTs is shown in Figure 4. The incident heat flux on a PT can be calculated from a heat balance using the following relation [Putorti, 2015]:

$$q_{inc}^{"} = \sigma \cdot T_{PT}^{4} + \frac{(h_{PT} + K_{cond})(T_{PT} - T_{\infty})}{\varepsilon_{PT}} + \frac{\rho_{ST} \cdot C_{ST} \cdot \delta \cdot \left(\frac{\Delta T_{PT}}{\Delta t}\right)}{\varepsilon_{PT}} \quad (4)$$

where q_{inc}'' is the incident heat flux, σ is the Stefan-Boltzmann Constant, 5.670×10^{-8} W/(m^2·K^4), TPT is the temperature of the plate (K), h_{PT} is the convection heat transfer coefficient, 10 W/(m^2·K), K_{cond} is the conduction correction factor determined from NIST cone calorimeter data, 4 W/(m^2·K), T_{∞} is the ambient temperature (K) as measured by a bare bead thermocouple near the plate thermometer shielded from the radiation, δ is the alloy plate thickness, 0.79 mm, and Δt is the data acquisition time step of 1 s. Values specified by the alloy manufacturer were used for the plate emissivity (ε_{PT} =0.85 at 480°C), the alloy plate density (ρ_{PT}=8470 kg/m^3), and the plate heat capacity (C_{ST} = 502 J/kg·K at 300°C).

Figure 4. A photo of the front of the 10 cm x 10 cm modified plate thermometer.

At each PT location, the gas temperature was also measured, as required by Equation 4. The gas temperatures were measured with K-type thermocouples fabricated from 0.51 mm diameter (24 AWG) wire. Table 3 lists the locations of the PTs relative to the center of each tree. Each tree was located under the center of the 13.8 m × 15.4 m canopy hood. The same Z, R, and Theta definitions used for Table 2 pertain to Table 3. Data labels are also included.

Table 3. Plate thermometer locations.

Direction Relative to Tree	Radius, R (m)	Height, Z (m)	Theta (°)
West	2.00	0.2	276.2
West	2.00	2.3	276.2
West	2.00	4.5	276.2
West	2.95	0.2	256.5
West	2.95	2.3	256.5
West	2.95	4.5	256.5
East	2.04	0.2	100.5
East	2.04	2.3	100.5
East	2.04	4.5	100.5
East	2.99	0.2	80.3
East	2.99	2.3	80.3
East	2.99	4.5	80.3

2.3.5. Yields of Exhaust Products

Bryant and Bundy [2019] describe the gas analysis which is part of the calorimetry system. Gas was extracted from the exhaust stream and the concentration of CO and carbon dioxide (CO_2) were measured using non-dispersive infrared analyzers [Bryant and Bundy 2019]. Soot yield was determined using a laser extinction measurement across the exhaust duct following the methodology of Mulholland et al. [2000] using a specific extinction coefficient of 8.7 m^2/g.

2.3.6. Visual Record

Three video cameras (Canon models XA40 and XA60) recorded the fire at 30 frames/s and a 1920 x 1080 pixel resolution. An XA40 and an XA60 both faced north toward the center of the tree with the XA40 recording the tree and the XA60 angled at about 45° (above horizontal) to record the fire plume and the exhaust duct. The two north-facing cameras were located 8.7 m due south of the center of the tree. Another XA60 camera was aimed from the southeast of the tree positioned about 17.5 m southeast of the tree. This video camera was mounted 3.1 m above the tree stand. A webcam was positioned 0.4 m above the tree stand and 2.9 m from the tree near the west column to allow close observation of the burner to determine ignition quality. The video cameras' locations, orientations (relative to horizontal), and settings are listed in Table 4.

Table 4. Video camera positions and settings.

Model	Location	Angle (deg)	f Stop	Shutter Speed (1/s)
Tests 1 – 4				
XA30	8.7 m south	0	2.8	1/1200
XA60	8.7 m south	45	4.0	1/1200
XA60	12.5 m southeast	0	2.6	1/1600
Tests 5 & 6				
XA30	same as above	0	2.8	1/1200
XA60	same as above	45	4.0	1/1200
XA60	same as above	0	4.0	1/1200

A digital still camera (Canon model 80D) was used to capture views of the experimental setup and trees before, during, and after each test. The camera exposure settings were set for automatic. During the ignition and intense burning period, the camera operator had to photograph the tree from the southeast direction about 20 m from the tree.

LED lights were positioned at (Z, R) equal to (0.6 m, -8.7 m) and (-4.6 m, -8.7 m), where Z is the distance from the floor and R is the distance from the duct/tree central axis (see Figure 2). The cameras and data acquisition results were synchronized to better than 2 s. The locations of the lights and cameras relative to the tree and other instrumentation are shown in Figure 2.

2.3.7. Photogrammetric Characterization

Tree geometry was characterized using photogrammetry, which enabled 3-dimensional (3D) reconstruction of the tree crown. This is particularly relevant for detailed fire modeling efforts where individual linear measurements (e.g. height, width) may not be sufficient to characterize the spatial distribution of biomass. The measurements were conducted using a tablet computer equipped with a 12 MP camera and the Scaniverse photogrammetry software (app). At least three orbits of each tree were completed, orienting the camera at different heights and angles to capture sufficient perspectives for photogrammetric reconstruction. For the tallest trees, a scissor lift was used to include an orbit at sufficient elevation to adequately view the tree top.

The output of the photogrammetric scan was in the form of a 3D point cloud which was manually cropped to contain only the tree, as shown in Figure 5a. These points represent only a subset of individual branch and needle locations, and the density was not sufficient to create a detailed wireframe mesh. Instead, they were used to create a voxelized representation where voxels on a predefined rectilinear mesh are filled in locations that contain points of the cloud (Figure 5c). A 5 cm voxel size was selected to be commensurate with possible mesh size for a fire model while also considering the uncertainty associated with the point cloud. Further exploration of voxel size is provided in Appendix F. Similar voxelization methods, based on lidar-derived point clouds, have been employed to provide vegetation geometry for fire modeling [Marcozzi et al., 2023].

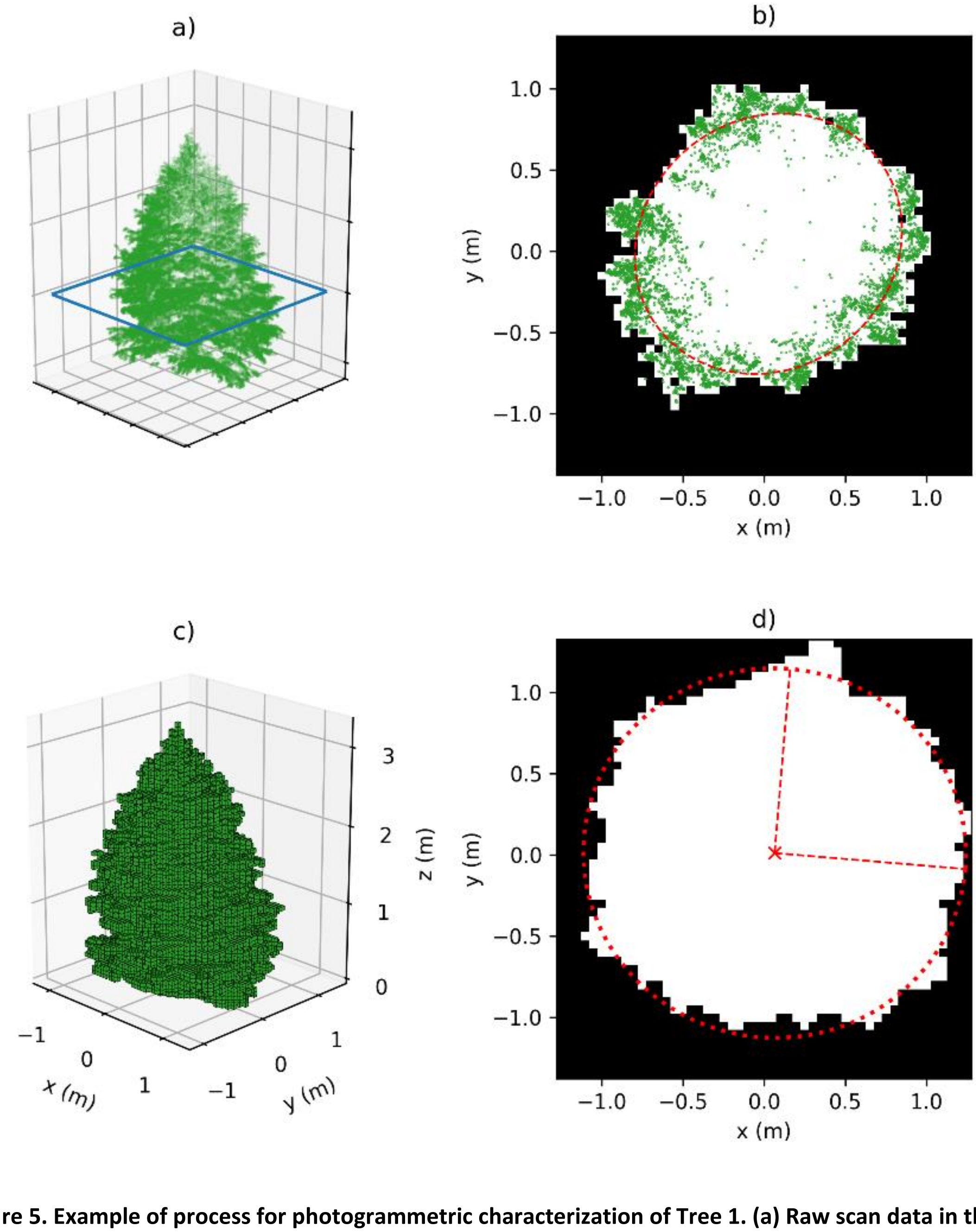

Figure 5. Example of process for photogrammetric characterization of Tree 1. (a) Raw scan data in the form of a 3-dimensional point cloud. (b) A horizontal slice (blue plane in (a)) of voxels containing points. Voxels inside an ellipse fit to the point cloud, using total least squares, are also filled. (c) Voxelized representation of the whole crown volume. (d) Major and minor crown radius were determined by fitting an ellipse with the same normalized second central moment as the projection of the voxelized crown geometry in the z-direction.

Because the photogrammetry cannot penetrate the dense crown, there are few points registered in the internal crown space. To obtain a total crown volume, an ellipse is fit to the point cloud contained in each horizontal slice of voxels using total least squares [Halır and Flusser, 1998]. Values within the ellipse are filled, as well as any remaining voxels which are completely surrounded by vegetation containing voxels. An example of this process is shown in Figure 5b,c.

In addition to computing volume, this method was used to determine tree height (difference between maximum and minimum voxel location in z-direction). An ellipse with the same normalized second central moment as the projection of the voxelized crown geometry in the z-direction was also used to determine a major and minor crown radius. An example is shown in Figure 5d. Results of the tree geometry characterization are given in Table 5.

Table 5. Tree dimensions determined from photogrammetry using a 5 cm voxel size. Uncertainties are reported as the combined expanded (k = 2) uncertainty, representing a 95 % confidence interval[a].

Tree	Height (m)	Major Crown Radius (m)	Minor Crown Radius (m)	Crown Volume (m^3)	Dry Fine Fuel Bulk Density[b] (kg/m^3)
1	3.30 ± 0.11	1.18 ± 0.11	1.14 ± 0.11	5.36 ± 0.62	1.21
2	3.55 ± 0.11	1.08 ± 0.11	1.03 ± 0.11	4.65 ± 0.60	1.80
3	4.20 ± 0.11	1.41 ± 0.11	1.28 ± 0.11	8.08 ± 0.88	1.54
4	3.95 ± 0.11	1.18 ± 0.11	1.06 ± 0.11	5.69 ± 0.68	1.93
5	5.85 ± 0.11	1.52 ± 0.11	1.39 ± 0.11	14.73 ± 1.32	1.66
6	5.7 ± 0.11	1.44 ± 0.11	1.38 ± 0.11	12.90 ± 1.28	1.73

a. See Appendix F for more detail.

b. Dry fine fuel mass is an approximation. Using data from Mell et al. [2009], it's estimated that 45% of the dry initial tree mass was fine fuel, that is foliage and branches with diameters of 10 mm or less.

2.4. Early Test Preparation

The Douglas-fir trees were delivered bound in twine. Before unwrapping each tree, they were lifted upright and mounted on a plywood stand (described in Section 2.4.1). The trunk of the tree was lowered into the trunk box on the center of the stand and the twine was removed. Four wooden supports were attached from the stand to the tree to provide bracing.

Before testing, a method of ignition was devised to protect the staff from the large, quickly growing fire. A hexagonal (roughly circular), non-premixed natural gas line burner was assembled and tested with various igniter methods. Igniter development and burner testing was performed before the first tree experiment and in between subsequent experiments to improve its performance.

Prior to each experiment, photographs of the tree were taken from various directions and the photogrammetry described in Section 2.3.7 was performed. Just before the experiments, samples of branch tips were collected for moisture content measurement.

2.4.1. Tree Stands

The trees were mounted on tree stands which in turn were placed on the load cell platform. The load cell platform consisted of a 1.83 m by 1.22 m cement board (1.3 cm thickness) on top of a plywood sheet of the same area (1.83 cm thickness). The two layered boards rested on wooden support beams (8.9 cm square cross-section) which spanned each pair of load cell modules on the north and south sides of the setup.

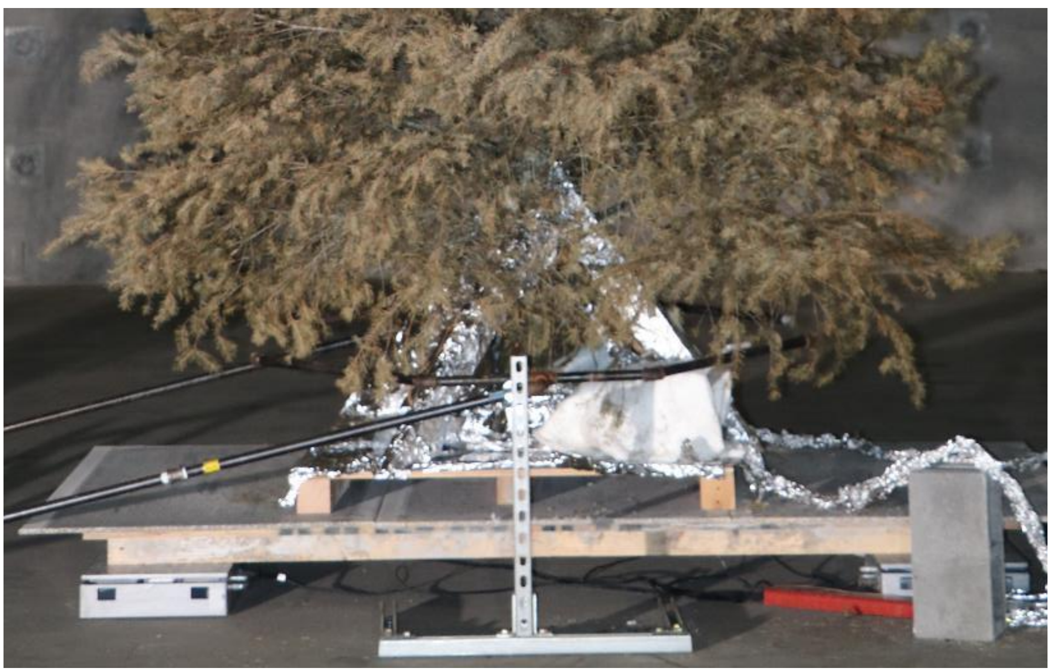

Figure 6. A photograph of the tree stand on the load cell platform.

Each tree stand consisted of two (nominal) 4 in × 4 in (8.9 cm square cross section) boards and a (nominal) 2 in × 4 in (3.8 cm × 8.9 cm cross section) board supporting a sheet of (nominal) ¾ in (1.83 cm) plywood. A box to hold the tree trunk was fabricated from 2 × 4 boards attached to the center of the plywood sheet base (see Figure 7). Four 2 × 4 boards were used to support the tree vertically and were attached at angles to the stand base and the tree. The lengths and angles of the support boards were adjusted for different tree heights. Aluminum foil was used to cover accessible portions of the 2 × 4s and base prior to each burn.

Figure 7. A photograph of a plywood tree platform prior to mounting of the tree.

2.5. Ignition Method

The trees were ignited with a hexagonally shaped natural-gas burner. The burner was ignited with remote spark ignition system which evolved during the course of the experimental series. The burner and spark igniters are described in the following sections.

2.5.1. Burner Description

All of the burner stages consisted of two three-sectioned halves made of series of 33 mm (1.32 in) OD (“1 in”) pipe sections leading from the natural gas supply to 27 mm (1.05 in) OD pipe sections that had 0.32 mm (1/8 in) diameter holes drilled every 2.5 cm (1 in) through the upward facing pipe and elbow connector surfaces to allow fuel gas to exit and create numerous small flames along the length of the burner. The two burner halves and their supply pipes, connected at the center sections, were separately supported by Unistrut stands. The burner was disassembled for the tree to be placed on the load cell and reassembled with the two halves forming an irregular hexagon.

- The burner was positioned below the bottom tree branches, as possible, such that the 10 cm to 20 cm (4 in to 8 in) burner flames would impinge on most of the branches. The burner design was changed as needed for the larger trees to ensure that the igniter flames were under the lowest branches. A photograph of the smallest version of the burner is shown in Figure 8. Figure 9 shows the same early version of the burner with the flames ignited. For larger tree heights and widths, the burner had to be widened with sections of pipe added to the supply “T” at the left of Figure 8. The two halves then had gaps between them. For the largest trees, when the gaps became too wide and burner flames were not present to ignite the branches above the gaps, additional pipe sections with holes were added to the burner. Photos of the burner arrangement are shown in Appendix A.

Figure 8. The first version of the burner used for the shortest trees.

Figure 9. The early version of the burner with flames ignited.

2.5.2. Ignition Description

A set of four spark igniters was used to ignite the natural gas burner. The igniter system consisted of an activation switch, a power supply, low-voltage extension wire, coil packs, and high-voltage extension wire. The power supply was a 5 V model with a 10 A capacity. The low voltage extension wire carried the current from the power supply and switch about 12 m from the control area in the adjacent laboratory space to the burner. At the burner, the low voltage wires were connected to the four 2 A coils located near the centers of four burner sections. At each coil, high voltage wires were connected with the ends placed above the burner holes with gap spacing on the order of 5 mm. The coil packs and high- and low-voltage wires were all protected from flame radiation by ceramic fiber blanket and aluminum foil where appropriate.

Table 6 provides a summary of the average igniter power, duration, and total energy used in each of the tests. The burner flames were maintained on the tree for approximately 10 s before the natural gas supply was shut off.

Table 6: The average igniter power, its duration, and the total energy applied to ignite the trees.[a]

Test	Igniter Power (kW)	Igniter Duration (s)	Igniter Energy (MJ)
1	130 ± 5 %	10 ± 10 %	1.3 ± 15 %
2	130 ± 5 %	10 ± 10 %	1.3 ± 15 %
3	130 ± 5 %	10 ± 10 %	1.3 ± 15 %
4	130 ± 5 %	10 ± 10 %	1.3 ± 15 %
5	165 ± 5 %	10 ± 10 %	1.7 ± 15 %
6	165 ± 5 %	10 ± 10 %	1.7 ± 15 %

a. Uncertainties are reported as the combined expanded (k = 2) uncertainty, representing a 95 % confidence interval.

2.6. Test Procedure

Shortly before each tree test, the burner igniters were tested. For the initial tree tests, the igniters were tested without the tree in place. It was found that the process of putting the tree in place and repositioning the burner and spark igniters diminished their performance during the experiments. Thus, in later experiments, the spark igniters were tested with the tree in place, but without any gas flow and with the igniters shielded to prevent inadvertent ignition of the tree branches by the sparks.

Natural gas was run through the burner lines for several seconds to charge the lines and mitigate non-symmetric ignition. The gas flow was opened 1 s prior to the spark igniters being turned on. The gas flow was maintained for 10 s before the valve was shut.

2.7. Post-Test Procedure

At the end of each experiment, several measurements were made prior to removing the burned tree. Photographs of the tree were taken from several sides. A photogrammetry record was created of the burned tree which rendered a three-dimensional model. Any branches or debris that was separated from the tree during burning were placed on the stand to obtain a final mass of the tree that was not consumed in the fire. The trunk diameter as a function of height above the tree base was determined using calipers, averaging two measurements taken at right angles to each other. For two trees, the diameters of the burned branch tips and their height above the tree base were measured using calipers. The results of the post-burn tree branch and trunk measurements are described in Section 3.5.

3. Results and Discussion

3.1. Brief Summary of Each Experiment

The fires burned very quickly with the period between ignition and peak fire size on the order of 5 s to 10 s. After the peak HRR, the fire size diminished over about the next 10 s. Once the flames self-extinguished, the tree was mostly in a glowing mode with typically just a few lower branches flaming for less than a minute.

The quality of the burner ignition (symmetric versus non-symmetric) and the degree of flame interaction with the lowest and outer branches strongly influenced the fire spread behavior. The first of each pair of trees of increasing size was less successful in attaining symmetric ignition, leading to less complete burning than the second of each pair. A brief description of the ignition quality, burning times, and fire spread is provided in Table 7.

Table 7. Summary of experimental observations, including ignition and fire spread.

Test	Ignition Quality	Fire Spread Description
1	Non-symmetric.	Burner failed to ignite several lower branches on the east side and a few on the northwest and southwest. Significant amount of protracted burning and a significant amount of unburned mass.
2	Nearly symmetric, but south half of burner ignited 2 s late.	Despite uneven ignition, most of tree still ignited. A few lower branches on southwest and west sides did not burn.
3	Non-symmetric; burner too far inward to ignite outer branches.	Bottom third of outer branches on the east side did not burn. Bottom 2/3 of outer branches on the west side did not burn.
4	Nearly symmetric.	A few low branches on the west and very low branches on the north and east sides didn't ignite. Most of tree burned.
5	Non-symmetric south half of burner did not ignite.	Fire spread more slowly and downward on the south side. Eventually, most of tree burned except a few lower, outer branches on the south, east, and north sides.
6	Nearly symmetric, but south half of burner ignited 2 s late.	Nearly all branches consumed. Only one small lower outer branch on the south side remained.

3.2. Mass Loss

The post-fire residual tree mass is associated with the tree trunk and large portions of unburned branches. The moisture content of the trees was sampled before the tests and after the tests in a charred region of the base of the trunk using a 3/8" (9.5 mm) hole saw. The samples were then measured using the moisture analyzer. On average, the moisture content of the charred trunk was measured as 21.4 % ± 2.9 % after the tests, which was about a factor of 1.03 lower than before the tests. This represents an insignificant difference if the uncertainty of the measurements is considered. For this reason, the moisture content of the residual mass is assumed to be unchanged from its pre-test value.

The dry basis fuel mass loss (Δm) was estimated by subtracting the specimen's water mass from the total mass loss measured using the load cell ($\Delta m_{measured}$), assuming the initial water remains in the residual mass of the post-fire tree:

$$\Delta m = \Delta m_{measured} \times (1 - \mathrm{MC}) \tag{5}$$

where MC is the dry-based moisture content of the specimen listed in Table 1. The value of $\Delta m_{measured}$ was calculated as (m_e - m_i), where m_i and m_e are the initial and final load cell masses in the fire test, respectively. Measurements of the trunk moisture content after the experiment are consistent with the assumption that MC is unchanged by the fire.

A heat of combustion on a per-oxygen basis of 13.23 kJ/g ± 0.66 kJ/g has been suggested as applicable for cellulosic materials with a range of stoichiometric oxygen-to-fuel mass ratios, ranging from pure cellulose to various chars [Dietenberger, 2021; Dietenberger, 2002].

The value of the net heat of combustion per unit fuel mass ($H_{c,net}$) was calculated from literature value for the gross heat of combustion (which is typically provided by a bomb calorimeter following, for example, ASTM 2019). The gross heat of combustion is then converted to a net value using the formula:

$$H_{c,net} = H_{c,gross} - 21.96h \tag{6}$$

where h is the mass fraction of hydrogen in the dry fuel, and the correction assumes that water formed by combustion remains as a vapor. The composition of 35 different vegetation samples from 4 references was evaluated with the average hydrogen mass fraction found to be 6.1 % with a relative standard deviation of 12 % [Simeoni et al., 2011; Safdari et al., 2018; Leroy et al., 2009; Susott et al., 1975]. The net heat of combustion for Douglas-fir was then determined to be 21 kJ/g [Susott et al. 1982]. Although the gross heat of combustion is often not reported with an uncertainty, the standard deviation of 6 values reported for Douglas-fir fires yielded 3 %, which is a relatively narrow value [Hurley, 2016; Parker and Levan, 1989; Susott, 1982]. Table 8 presents a summary of the experimental results organized by specimen number, including the total fuel mass loss corrected for water (Δm), the residual mass percentage, the test duration, peak HRR, time to peak HRR, and the total heat released (THR). The THR is the measured heat release rate measured via oxygen consumption calorimetry integrated over the entire test duration. The residual mass ratio (m_e / m_i) is the mass of the burnt specimen at the end of the test divided by the specimen's initial mass. Appendix E discusses rescaling the HRR profile to correct for the calorimetry system's time response.

The discussion below emphasizes the magnitude of the total heat released by the fire (THR) and its peak HRR. The former parameter quantifies energy released by the fire, whereas the latter is an indicator of fire hazard as the peak HRR of a single item burning can strongly influences the rate of fire spread and growth [Babrauskas 1992].

Table 8. Summary of test results including the fuel mass loss corrected for water content (*Δm*) and post-fire residual mass percentage. The peak HRR, time to peak HRR, and the total heat release (THR) measured by oxygen consumption calorimetry are also listed. Uncertainties are reported as the combined expanded (k = 2) uncertainty, representing a 95 % confidence interval.

Test	Δm [kg]	Residual Mass [%]	Peak HRR[a] [MW]	Time to Peak HRR [s]	THR [MJ]
1	9.32 ± 2.48	35	7.4 ± 0.8	7 ± 4	168 ± 10
2	7.77 ± 1.77	58	12.2 ± 1.3	5 ± 4	159 ± 9
3	8.10 ± 2.69	71	8.8 ± 0.9	9 ± 4	153 ± 9
4	11.22 ± 2.67	54	13.7± 1.4	8 ± 4	218 ± 13
5	27.95 ± 5.90	49	33.5 ± 3.6	9 ± 4	579 ± 31
6	23.95 ± 5.65	51	36.8 ± 3.9	7 ± 4	601 ± 30

a. Due to the fast fire growth and the calorimetry system's relatively slow time response, the peak HRR uncertainty is likely underestimated as discussed in Appendix E.

3.2.1. Heat Release Rate and Total Energy

The figures showing the heat release rate (HRR) in time for each tree specimen are compiled in Appendix B. The HRR was measured in the exhaust hood using the Oxygen consumption (O_2) calorimetry methodology outlined by Bryant and Bundy [2019]. Additionally, the HRR was determined using the measured mass loss rate (MLR) such that:

$$HRR_{MLR} = \dot{m}\, H_{c,net} \tag{7}$$

where $\dot{m}$ is the dry fuel mass loss rate (corrected for the moisture content listed in Table 1), and $H_{c,net}$ is the net heat of combustion of Douglas-fir taken as 21 kJ/g following Susott [1982] (discussed in Section 3.2 above). Figures B1 to B6 in Appendix B show that in all the tests, the mass loss rate estimate (Equation 7) of the peak HRR was larger than the peak based on O_2 calorimetry, attributed to the faster time response of the load cell instrumentation. Details of the calorimetry system and characterization of its time response are found in Bryant and Bundy [2019]. A correction method to address the time response of the HRR calorimetry measurement system using the load cell and heat flux measurements is discussed in Appendix E.

Figure B1 to Figure B 6 in Appendix B also show that Trees 1, 3, and 5, which had non-symmetrical ignition and thereby a slightly longer time to burn, featured better agreement between the two HRR determination methods during the post-peak period than Trees 2, 4, and 6, which ignited symmetrically and quickly consumed the whole tree. The reason for this subtle difference in the in the post peak transient profiles is at least partially due to the slower burning of the trees with the non-symmetric ignitions. This is seen, for example, in the difference in the times between the HRR peaks determined by the mass loss rate and the calorimetry for each of the tree pairs (Trees 1 and 2, Trees 3 and 4, and Trees 5 and 6), which is larger for the trees with non-symmetric ignitions. Another possible factor may be related to other factors such as differences in the amount of smoldering or moisture loss. The non-symmetric ignition fires (Trees 1, 3, and 5) were slower burning, the tests were of longer duration, and a substantial amount of unburned foliage remained in the lower portions of the trees (see photos in Appendix A). There may have been relatively more mass loss associated with moisture evaporation for these tests, which would lead to larger values of HRR determined by the mass loss rate method (Equation 7). Differences in the fractional amount of smoldering combustion may have also played a role as smoldering combustion has a significantly larger heat of combustion than flaming combustion. Distinguishing between the heat release rate associated with smoldering and flaming combustion regimes is impossible from a practical perspective as both smoldering and flaming occur simultaneously on different sections of the trees during the fires.

The total heat release is determined by integrating the transient HRR measurements (see Figure B1 to Figure B 6) over the duration of the experiments. Figure 10 shows the results of such a comparison. The dotted line represents parity. For most of the trees (Trees 2, 3, 4, and 5), the difference in heat released between the two methods is less than 11 %. The average difference for all the trees is equal to 9.3 %.

A best fit line to the data leads to a non-zero intercept, which is non-physical. Yet, there is a trend in the data driven by Trees 1 and 3, which are above parity, and the largest of the fires, Trees 5 and 6, which are below parity. Trees 1 and 3 had non-symmetric ignitions (Table 7) and substantial amounts of unburnt foliage. Slow heating of the unburnt thin fuels on these trees may have caused disproportionate moisture loss without contributing to the energy release, thereby leading to a higher apparent HRR calculated from the mass loss rate estimation method.

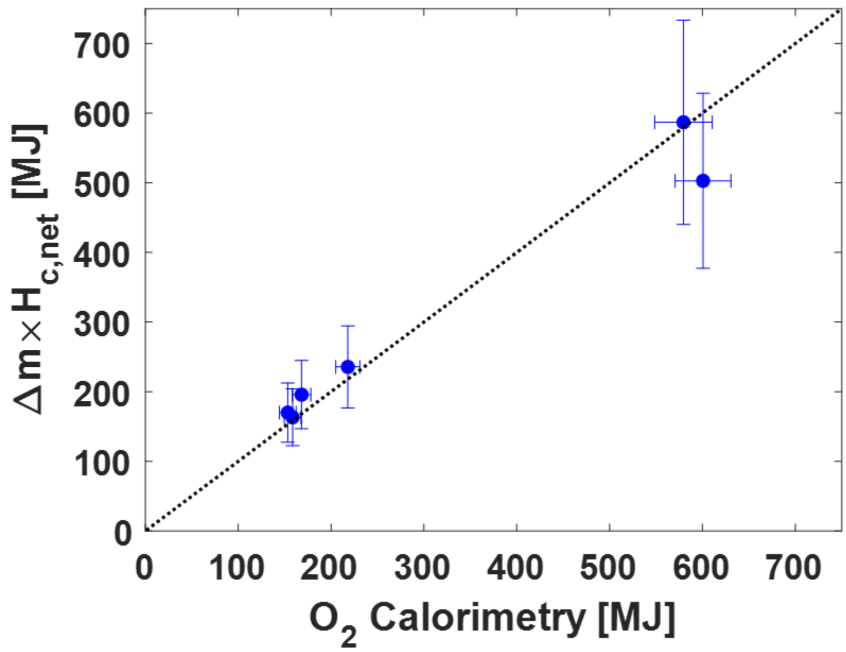

Figure 10. The total heat released determined from the total mass loss (corrected for water) versus the *O_2* consumption calorimetry. The dotted line represents parity, and the error bars represent the expanded combined uncertainties representing a 95 % confidence interval.

3.3. Heat Flux

3.3.1. Near-field Heat Flux

Peak heat flux values measured at various heights at 2 m and 3 m radial distance from the trees are presented in Table 9. Alongside the measurements from this study, the values from Mell et al. [2009] are given for comparison. The Mell et al. [2009] measurements were conducted at the same height and distance as this study for 2 m and 5 m tall trees. The complete heat flux measurements as a function of time from the radiometers and PTs are provided in Appendix D.

At the 2 m radial distance, the shorter trees in this study (Trees 1 and 2) featured similar peak heat flux values (within 4 % or better of each other) at the z = 2.3 m and 4.5 m heights. However, for the taller trees (Trees 3 to 6), higher peak values (from 9 % to 47 %) were generally observed at the 2.3 m height than the 4.5 m height. This trend is likely due to the view factor effect of the heat flux gauges, with the mid-height (z = 2.3 m) heat flux gauges capturing the bulk of the fire, while the highest gauges (z = 4.5 m) mainly captured the plume above the fire. Similarly, for the shorter trees, the z = 2.3 m and 4.5 m gauges measured similar heat fluxes likely since the bulk of the tree fire occurred between the 0.2 m and 2.3 m positions. At the 3 m radial distance, peak heat flux values were generally higher at z = 4.5 m measurement location for all tree heights.

The 2 m tall trees from Mell et al. [2009] had similar peak heat flux values to the shortest tree in this study (Trees 1), particularly at the z = 2.3 m and 4.5 m measurement locations (within 4.5 % to 13.5 %). Furthermore, the 5 m tall trees had a higher peak heat flux at the z = 2.3 m than at z = 4.5 m, in agreement with the observations in this study. Thus, the trends presented here match reasonably well with the trends observed from Mell et al. [2009] However, it is important to note that the measurements from this study represent a single tree, while the values from Mell et al. [2009] are the average of several tree burns of the specified height. Not just height and ignition symmetry influence the measured heat flux, natural variation and the amount of mass burned are also important.

Table 9. Peak heat flux measurements from the West column at 2 m and 3 m radial distance from the center. Similar measurements from Mell et al. [2009] are provided for comparison.

		r = 2 m [kW/m^2]			r = 3 m [kW/m^2]		
Height (m)	**Tree**	**z = 0.2 m**	**z = 2.3 m**	**z = 4.5 m**	**z = 0.2 m**	**z = 2.3 m**	**z = 4.5 m**
3.4 m	Tree 1	5.6±0.6	19.1±2.1	19.9±2.2	5.7±0.6	10.7±1.2	12.9±1.4
3.7 m	Tree 2	12.9±1.4	39.3±4.3	39.2±4.3	11.1±1.2	21.4±2.3	26.2±2.9
4.3 m	Tree 3	3.0±0.3	19.1±2.1	21.3±2.3	3.1±0.3	10.5±1.2	12.1±1.3
4.1 m	Tree 4	11.9±1.3	40.0±4.4	36.8±4.0	9.9±1.1	19.0±2.1	21.8±2.4
5.8 m	Tree 5	10.9±1.2	56.4±6.1	50.2±5.5	10.1±1.1	26.4±2.9	29.9±3.3
5.8 m	Tree 6	33.5±3.6	85.3±9.3	58.0±6.4	25.5±2.9	42.9±4.6	41.4±4.5
Mell et al. [2009]							
2 m	trees	12±3	20±3	23±3	6±3	10±3	12±3
5 m	trees	20±3	55±3	40±3	10±3	15±3	13±3

3.3.2. Far-field Heat Flux

The peak heat flux observed by the far field gauges at r = 12 m distance are plotted in Figure 11 as a function of the peak HRR. Trees 1 and 3 featured a large discrepancy between the measured peaks from the NW and SE locations. This discrepancy indicates anon-symmetric ignition, as either the front or back half of the tree burned more intensely, although it is not the sole indicator of an asymmetric fire as indicated by the results from Tree 5. Tree 5 was similar in size to Tree 6 (Table 1) and released a similar amount of energy (Table 8). However, in comparison to Tree 6, Tree 5 had diminished peak heat flux both in the near and far fields, indicative of a non-symmetric ignition. Figure B13 to Figure B18 show the heat fluxes measured at 10 m from the trees. As expected, the values of the peak heat flux measured at a distance of 10 m was significantly larger than the peak values at 12 m, with the ratio of the peak values approximately proportional to the inverse of the ratio of the square of the distance from the trees.

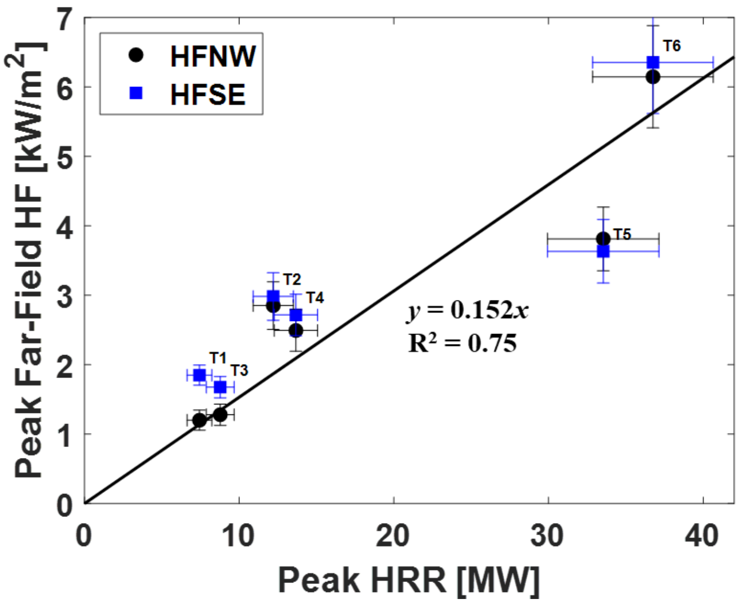

Figure 11. Peak far-field heat flux (at r = 12 m) from the northwest (HFNW) and southeast (HFSE) gauges plotted against peak heat release rate for each tree burn. A linear regression of all the data points is plotted as well. Trees 1 to 6 are labelled T1 to T6 in the figure. The error bars represent the expanded (k=2) combined uncertainties representing a 95 % confidence interval.

In the cases of fires with non-symmetric ignitions (Trees 1,3, and 5), the lower peak heat fluxes in both the near and far-field are due to the entire tree not burning simultaneously, but rather one half ignited first. The fire then propagated to the unlit region. This process caused instantaneous values (such as peak HRR and peak Heat flux) to be lower, but integrated values remain close to those of similar trees which ignited all at once.

3.4. Total Radiated Energy and Radiative Fraction

Figure 12 shows the TRE measurements as a function of the total heat released (THR). As expected, the figure shows a strong linear trend between the total heat released and the total radiated energy These results support the idea of a constant value for the radiative fraction over the range of fire sizes considered in this study.

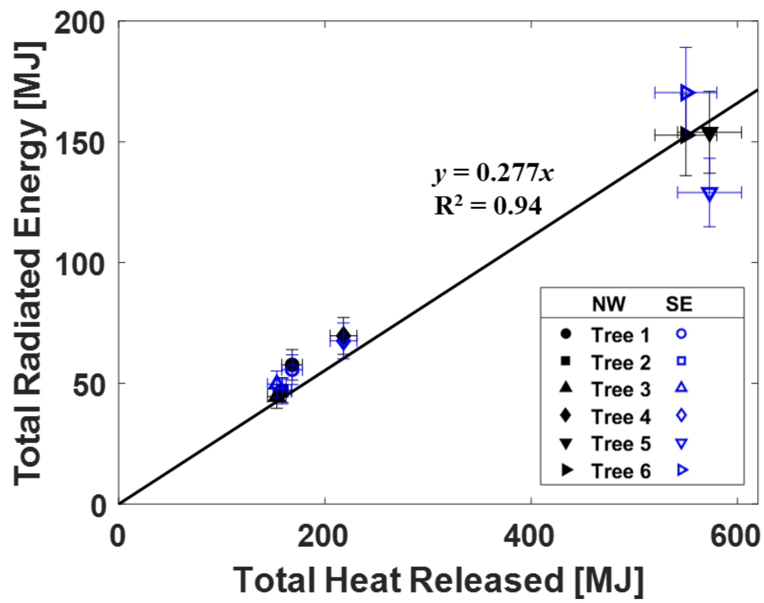

Figure 12. The total radiated energy as a function of the total heat released (THR) by the fire (from calorimetry). A linear regression of all the data points is plotted as well. The error bars represent the expanded (k=2) combined uncertainties representing a 95 % confidence interval.

Table 10 lists the measured total radiated energy (TRE) over the duration of the tests as defined in Equation 2 for each of the radiometers (NW and SE positions) at r = 12 m. Trees 1, 3, and 5 had non-symmetric ignition, so differences in the transient far-field radiative flux measurements might be expected as seen in Figures D13 and D15.

The table also lists the radiative fraction (χ_{rad}), which was estimated using the TRE data and Equation 3 (see Section 2.3.4). The value of χ_{rad} does not represent all the energy radiated by the specimen as some fraction of the energy was obstructed by the specimen itself. As can be seen in Figure 12, there is fair agreement between the two far-field heat flux gauge locations (NW and SE) with the difference ranging from 0.7 % (Tree 2) to 19.2 % (Tree 5). The larger trees tended to have higher discrepancies between the two locations. The average value and standard deviation of χ_{rad} was 0.30 ± 0.03. There was no apparent difference between the trees with symmetric and non-symmetric ignition. The results indicate that χ_{rad} is approximately independent of fire size for these dry Douglas-firs. Sung et al. [2024] observed a decrease in χ_{rad} with moisture content for fires involving 1 m to 2 m tall Douglas-fir trees. For trees with moisture content less than 15 %, like those in this study, Sung [2024] found that χ_{rad} was equal to 0.28 ± 0.04 consistent with the results in Table 10.

Table 10. The total radiated energy determined from the far-field NW and SE heat flux gauges and the radiative fraction, χ_{rad}. The average uncertainty of the TRE and χ_{rad} is 11 % and 17 %, respectively.

Tree	TRE_{NW} [MJ]	TRE_{SE} [MJ]	χ_{rad}
1	57.4	55.6	0.34
2	46.9	46.6	0.29
3	44.4	49.6	0.31
4	69.6	67.6	0.31
5	153.7	129.0	0.25
6	152.4	170.3	0.29

Figure 12 shows the TRE measurements as a function of the total heat released (THR). As expected, the figure shows a strong linear trend between the total heat released and the total radiated energy.

3.4.1. Yields of Exhaust Products

Table 11 lists the total soot, CO, and CO_2 yields on a mass basis. The measured soot and CO yields varied from about 0.003 to 0.005, and from 0.07 to 0.09, respectively. There were only small differences in the yields among the larger and smaller HRR fires, nor among the fires that had symmetric or non-symmetric ignitions. The largest soot yield was measured as 0.0050 ± 0.0007 during Test 3. Considering all the tests, the average values and standard deviations of the soot and CO yields were 0.0043 ± 0.0009 and 0.0809 ± 0.0070, respectively.

Table 11. Soot and Carbon Monoxide (CO) yields. Uncertainties shown are the expanded (k = 2) uncertainties, which represent a 95 % confidence interval.

Test	Soot Yield [g/kg]	CO Yield [g/kg]	CO_2 yield [g/kg]
1	4.69 ± 0.60	75.7 ± 2.7	1.46 ± 0.05
2	3.69 ± 0.53	73.4± 5.5	1.75 ± 0.13
3	4.99 ± 0.71	81.4± 6.0	1.76 ± 0.13
4	3.25 ± 0.46	82.7± 6.2	1.77 ± 0.13
5	4.91 ± 0.70	91.2± 6.6	1.41 ± 0.10
6	3.14 ± 0.45	72.9± 5.3	1.62 ± 0.12

The yields in these fires are similar to those of Sung et al. [2024], who reported soot and CO yields in 0.8 m to 1.8 m Douglas-Fir trees as 0.0041 ± 0.0025 and 0.089 ± 0.015. Tewarson [2016] reports that the CO yield from solid wood small (10 cm) Douglas-fir samples burning in air in the Fire

Propagation Apparatus (FPA) is 0.004 kg/kg, which is about a factor of two lower than the values in Table 10 for these large Douglas-fir trees. This difference is not surprising as the FPA uses very small samples experiencing a constant heat flux in a "simulated" fire condition for the solid wood samples. The yields were more like a lightly sooting 34 kW propane fire [Falkenstein-Smith, 2023]. Figure 13 shows the ratio of the CO yield to the soot yield as a function of the THR. Data for 1.5 m tall Douglas-fir trees with THR greater than 50 MJ from Sung et al [2024] are also shown. A line in the figure shows the average ratio of the yields for all the data at a value of approximately 20.

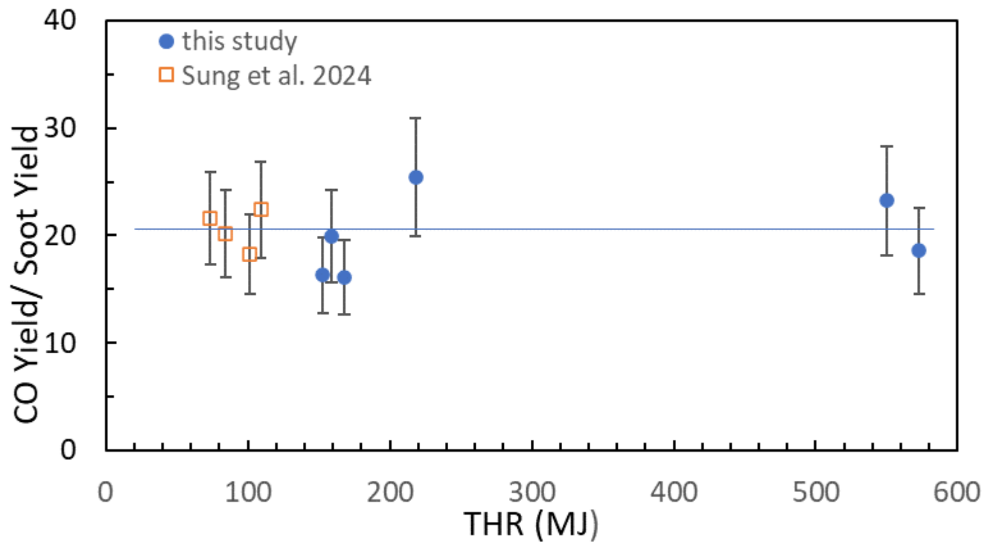

Figure 13. The ratio of the CO yield to the soot yield plotted as a function of the THR. Data from Sung et al. [2024] are also shown. A line showing the average value is also shown. The error bars represent the expanded (k=2) combined uncertainties representing a 95 % confidence interval.

3.5. Post-test Branch Tips

After the fire tests in the dry Douglas-fir trees, nearly all the needles were gone, and the tree trunk and branches had a thin (~1 mm) carbonaceous layer. Many of the branch tips appeared to have burned. Measurements of the post-fire branch tip diameter as a function of distance above the stand base are shown in Figure 14 and Figure 15 for Trees 4 and 6, respectively. The results show that the branch tip diameters varied from about 3 mm to 1.2 cm. In general, there was large scatter in the data. For Tree 6, a linear regression of the branch tip diameters yields a positive slope albeit with a relatively small R2 value (=0.37). Tree 6 was almost 6 m tall, significantly taller than the 4 m tall Tree 4 (see Figure A 4 and Figure A 6). We speculate that with its much larger plume, the top branches of Tree 6 would have experienced larger vertical plume velocities and higher heat fluxes. This would have led to more intense burning higher in the tree and consequently larger branch tips as more of the smaller tips burned away. Tree 4 (Figure 14) shows that the branch tip diameters increased with distance above the base like Tree 6, but near the burned tree top, the branch tips decreased in diameter towards the top of the tree. Further research is needed to examine this phenomenon.

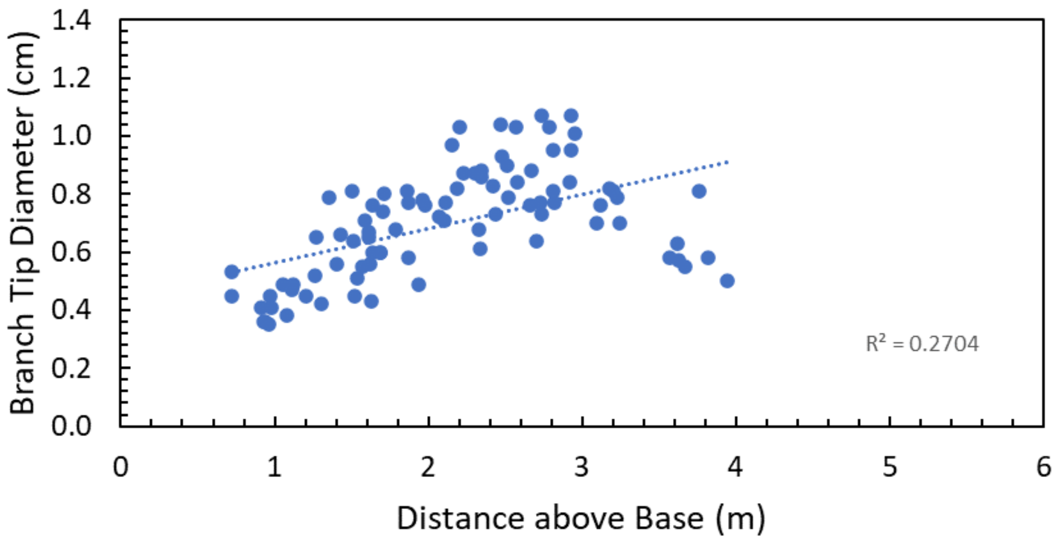

Figure 14. The branch tip diameter as a function of distance above the tree stand base for Tree 4.

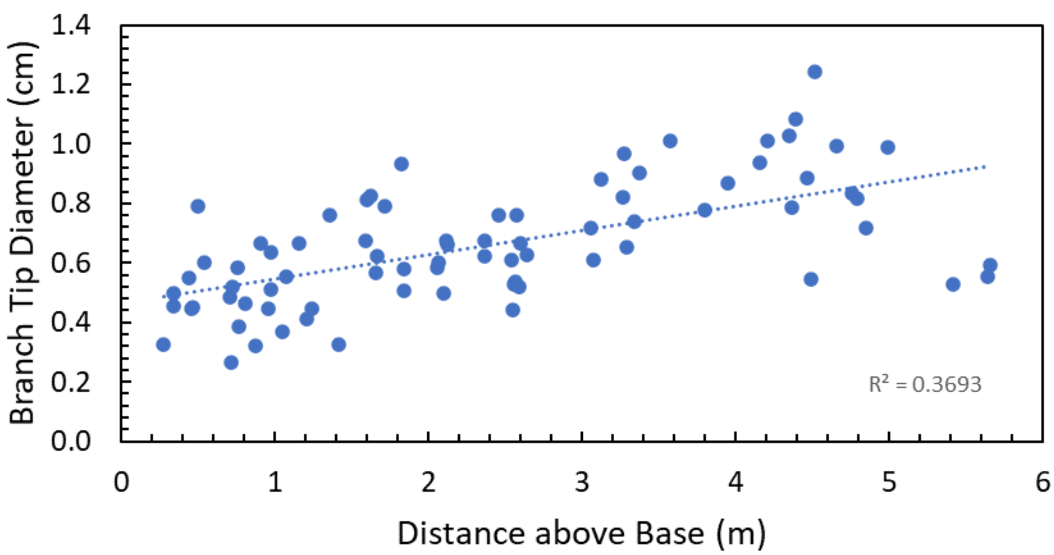

Figure 15. The branch tip diameter as a function of distance above the tree stand base for Tree 6.

4. Summary and Conclusions

A series of experiments are reported on the burning behavior of dry Douglas-fir trees between 3 m and 6 m tall. The trees were characterized by measuring their moisture content and by photogrammetry, which provided information on the gross details of the tree structure. The moisture content of the trees on a dry basis varied from 8 % to 13 %. The appearance of the trees before, during, and after burning was captured by video and still photographic cameras from many perspectives. The fire measurements reported include the transient, peak, and total heat release rates, the yields of CO and soot, the mass loss and the near and far-field radiative flux. Measurements of the heat flux to the surroundings from the specimens were used to estimate the radiative fraction of the fires. The results provide unique calorimetric data which can be useful for development of design fire scenarios by fire protection engineers. A few previous studies have considered trees over 2 m tall, but none have provided such a complete set of global burning properties.

The measurement results characterize the global combustion properties of the specimens and offer insight on the burning behavior of the fires. A number of general findings from the study include the following:

- For some tree experiments, non-uniform ignition of the burner or poor contact between burner flames and foliage led to non-uniform ignition of some of the lower tree branches. The resulting asymmetric burning of the tree caused less foliage to become involved in the fire and produced lower peak HRR values compared to those produced by symmetric burning from uniform burner ignition and better burner flame-tree contact. For both symmetric and asymmetric tree ignitions, similar total mass loss was observed between trees of similar size despite differences in their temporal HRR curves, peak values, and even the apparent amounts of remaining unburned foliage.
- The profiles of the transient HRRs measured by calorimetry and those calculated from the product of the mass loss rate and the heat of combustion were significantly different, which is attributed to differences in the response times of the instrument systems. The rapidly growing fires push the limits of the NIST calorimetry system response, introducing uncertainties in the transient values. A first pass at a correction and calorimetry rescaling methodology is presented. This topic merits further study and characterization.
- The total heat release measured by calorimetry and the ideal heat release calculated from the product of the integrated mass loss rate and the heat of combustion were in agreement within experimental uncertainty. The average difference for all the trees from parity is equal to 9.3 %. There appears, however, to be a trend such that the total heat release calculated by calorimetry is larger than that calculated by the ideal heat release for the largest fires, with

the opposite true for the smaller fires, particularly for the trees with non-symmetric ignitions and substantial amounts of unburnt foliage. These trends may be related to assumptions made in the estimation of the total heat release values associated with invariant moisture content pre- and post-fire for all the trees regardless of the fire size. Differences in the fractional amount of smoldering versus flaming combustion may have also played a role.

- The trends of the near-field heat flux measurements at 2 m and 3 m from the tree center are consistent with the results from similar experiments reported by Mell et al. [2009].
- The radiative fraction, χ_{rad}, of the 3 m to 6 m Douglas-fir tree fires was estimated from the heat flux measured 12 m from the burning trees, yielding an average value and standard deviation of 0.30 ± 0.03, which was consistent with previous measurements on 1 m to 2 m Douglas-fir trees with moisture content less than 15 %.
- The ratio of the CO yield to the soot yield is nearly constant over a wide range of total heat release rates with an average value of about 20. The results are consistent with previous studies on smaller trees and as with radiative fraction there was no apparent dependence on tree size for these 3 m to 6 m Douglas-fir trees.
- Photogrammetry was used to characterize the gross details of the tree structure. This approach enabled a three-dimensional reconstruction of the tree crown. This provided volume estimates which are used to calculate crown bulk density, which is a key parameter in quantifying and modeling vegetation burning dynamics.
- The post-fire branch tip diameters were measured as a function of distance above the tree base. This type of information may be related to the local temperature and velocity field experienced by the trees during a fire, which could be useful to computational fluid dynamics fire models of tree burning. Further research on this topic may be of value.

The data generated from the study is available on the NIST Fire Calorimetry Database (FCD). The experiments reported here represent the first stage of a multi-phase project. Future experiments will address large tree fires with variable moisture content.

5. References

Accary G, Darido J, Morvan D (2024) Experimental and numerical investigation of a single-tree fire, *Journal of Fire Sciences* 42, 142-170. https://doi.org/10.1177/07349041231218967

ASTM International (2019) ASTM D5865/D5865M-19 -- *Standard Test Method for Gross Calorific Value of Coal and Coke,* ASTM International, West Conshoshocken, PA, USA. https://www.astm.org/d5865_d5865m-19.html

ASTM International (2024) ASTM E2067-24 -- *Standard Practice for Full-Scale Oxygen Consumption Calorimetry Fire Tests,* ASTM International, West Conoshoshocken, PA, USA. https://www.astm.org/standards/e2067

Babrauskas V (2016) Heat Release Rates in *The SFPE Handbook of Fire Protection Engineering* Hurley M (New York, NY, Springer), Vol. 1, Chapter 26, 5th Ed., 799-904. https://www.sfpe.org/publications/handbooks/sfpehandbook.

Babrauskas V, Peacock RD (1992) Heat Release Rates: The Single Most Important Variable in Fire Hazard, *Fire Safety Journal* 18, 255-272. https://doi.org/10.1016/0379-7112(92)90019-9

Babrauskas V, Chastagner G, Stauss E (2001) The Heat Release Rate Hazard of Christmas Trees, Chapter V in Flammability of Cut Christmas Trees, *International Association of Arson Investigators (IAAI) Annual General Meeting and Conference*, Atlantic City NJ (2001). https://doctorfire.com/pages/ChristmasTreeFires.pdf (accessed 10/30/2024)

Bigda K (2021) Christmas Tree Fire Safety Requirements, National Fire Protection Association (NFPA) , Quincy, MA. https://www.nfpa.org/news-blogs-and-articles/blogs/2021/11/12/christmas-tree-fire-safety-requirements (accessed 28 Oct. 2024).

Bryant R, Bundy M (2019) The NIST 20 MW Calorimetry Measurement System for Large-Fire Research, *NIST Technical Note 2077*, National Institute of Standards and Technology, Gaithersburg MD. https://doi.org/10.6028/NIST.TN.2077

Dietenberger M, Hasburgh LE, Yedinak K (2021) Fire Safety of Wood Construction, Chapter 18 in Ross R and Anderson JR (Eds) *Wood Handbook—Wood as an Engineering Material*, General Technical Report FPL-GTR-282, Madison, WI: U.S. Department of Agriculture, Forest Service, Forest Products Laboratory. https://www.fs.usda.gov/research/treesearch/62200

Dietenberger M (2002) Update for Combustion Properties of Wood Components, *Fire and Materials* 26, 25-267. https://doi.org/10.1002/fam.807.

Falkenstein-Smith RL, Sung K, Hamins A (2023) Characterization of Medium-Scale Propane Pool Fires, *Fire Technology* 59, 1865-1882. https://dx.doi.org/10.1007/s10694-023-01412-9.

Halır R, Flusser J (1998) Numerically stable direct least squares fitting of ellipses. In Proc. 6th International Conference in Central Europe on Computer Graphics and Visualization, WSCG, 98, 125-132, Plzen-Bory: Citeseer. https://api.semanticscholar.org/CorpusID:15772208

Hoehler MS, Bundy MF, DeLauter L, Materese R, Geršković L, García JR (2020) Fire Hazards of Dry Versus Watered Christmas Trees, NIST Technical Note 2131, National Institute of Standards and Technology, Gaithersburg, MD. https://doi.org/10.6028/NIST.TN.2131

Huskeflex Thermal Sensors (2024) SBG01 Water-Cooled Heat Flux Sensor technical information sheet. https://www.hukseflux.com/uploads/product-documents/SBG01_v2313.pdf (accessed 23 Nov. 2024).

Leroy V, Cancellieri D, Leoni E (2009) Relation between Forest Fuels Composition and Energy Emitted During Their Thermal Degradation, *Journal of Thermal Analysis and Calorimetry 96*, 293-300 https://doi.org/10.1007/s10973-008-9587-9

Marcozzi AA, Johnson JV, Parsons RA, Flanary SJ, Seielstad CA, Downs JZ (2023) Application of LiDAR derived fuel cells to wildfire modeling at laboratory scale, *Fire 6*(10), 394. https://doi.org/10.3390/fire6100394

McGrattan K, Hostikka S, Floyd J, McDermott R, Vanella M (2024) Fire Dynamics Simulator User's Guide, Version 6.9.1, NIST special publication 1019-6, Sixth Ed., National Institute of Standards and Technology, Gaithersburg, MD. https://pages.nist.gov/fds-smv/downloads.html

Mell W, Maranghides A, McDermott R (2009) Numerical Simulation and Experiments of Burning Douglas-fir Trees, *Combust Flame* 156, 2023-2041. https://doi.org/10.1016/j.combustflame.2009.06.015

Modarres M, Almeida M, Viegas DX (2024) Experimental and numerical fire behaviour analysis in Eucalyptus globulus trees, *International Journal of Wildland Fire*, 33(11). https://doi.org/10.1071/WF23131

Mulholland GW, Johnsson EL, Fernandez MG, Shear DA (2000) Design and testing of a new smoke concentration meter. Fire and Materials 24(5),231–243. https://doi.org/10.1002/1099-1018(200009/10)24:5<231::AID-FAM743>3.0.CO;2-N

Parker W J, Levan SL (1989) Kinetic Properties of the Components of Douglas-Fir and the Heat of Combustion of Their Volatile Pyrolysis Products, *Wood and Fiber Science* 21, 289-305. https://wfs.swst.org/index.php/wfs/article/view/1687

Pitts WM, Murthy AV, De Ris JL, Filtz JR, Nygård K, Smith D, Wetterlund I (2006) Round Robin Study of Total Heat Flux Gauge Calibration at Fire Laboratories, *Fire Safety Journal* 41, 459-475. https://dx.doi.org/10.1016/j.firesaf.2006.04.004

Putorti A (2015) Characterizing the thermal effects of High Energy Arc Faults. SMiRT 23 – 14th International Seminar on Fire Safety in Nuclear Power Plants and Installations (GRS-A-3845), Salford, UK.

Safdari MS, Rahmati M, Amini E, Howarth J E, Berryhill J P, Dietenberger M, Weise D R, Fletcher TH (2018) Characterization of Pyrolysis Products from Fast Pyrolysis of Live and Dead Vegetation Native to the Southern United States, *Fuel* 229, 151-166. https://doi.org/10.1016/j.fuel.2018.04.166

Simeoni A, Salinesi P, Morandini F (2011) Physical Modelling of Forest Fire Spreading through Heterogeneous Fuel Beds, *International Journal of Wildland Fire* 20, 625-632. https://doi.org/10.1071/WF09006

Schneider L, Betting B, Patterson M, Skowronski N, Simeoni A (2021) Experimental study of fire spread through discontinuous fuels without flame contact, Fire Safety Journal 120. https://doi.org/10.1016/j.firesaf.2020.103066

Sung K, Mueller E, Bundy M, Fernandez M, Hamins A (2025) Global Burning Properties of Little Bluestem, Excelsior and Douglas-fir, *NIST Technical Note (NIST TN) 2314*, National Institute of Standards and Technology, Gaithersburg MD. (to appear) https://doi.org/10.6028/NIST.TN.2314

Susott RA (1982) Characterization of the Thermal Properties of Forest Fuels by Combustible Gas Analysis, *Forest Science* 28, 404-420.

Susott RA, DeGroot WF, Shafizadeh F (1975) Heat Content of Natural Fuels, *Journal of Fire and Flammability* 6, 311-325.

Tewarson A (2016) Appendices in *The SFPE Handbook of Fire Protection Engineering* Hurley M (New York, NY, Springer), Vol. 1, Chapter 26, 5th Ed., pp 799-904. https://www.sfpe.org/publications/handbooks/sfpehandbook.

Wickstrom U (1994) The Plate Thermometer – A Simple instrument for reaching harmonized resistance tests, *Fire Technology* 30(2), 209-231.

Appendix A. Photos of Test Specimens Before, During, and After Testing

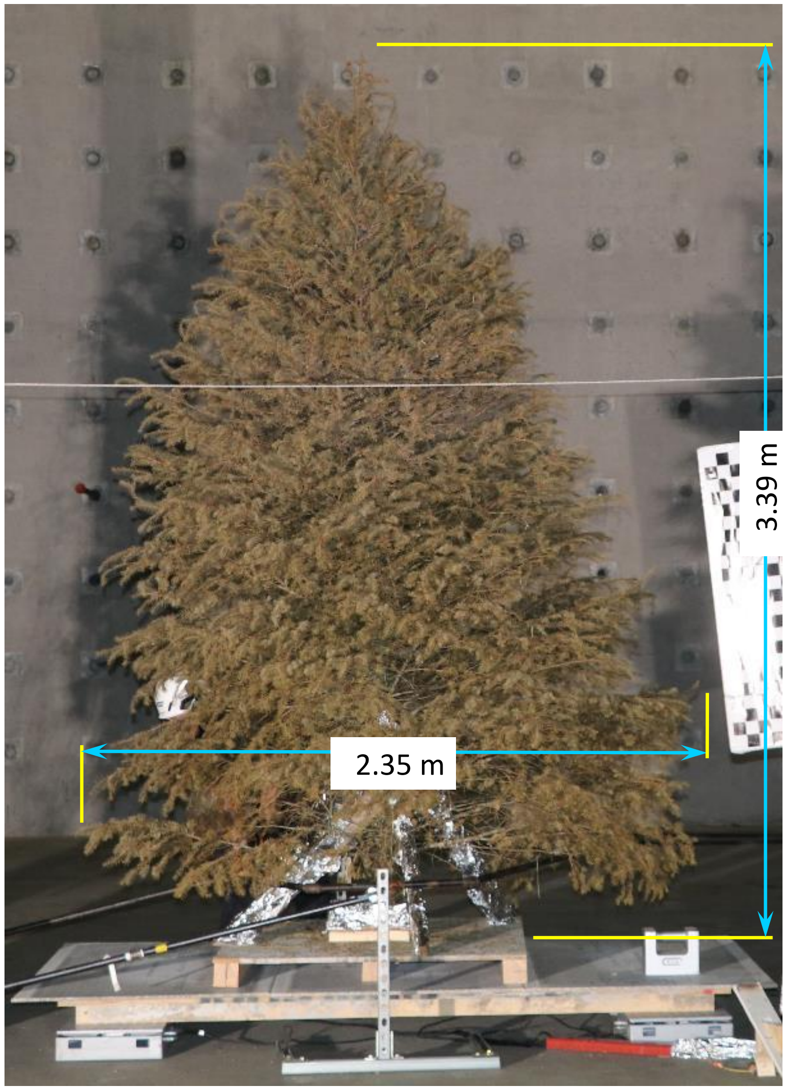

Figure A 1. Test 1 photo with dimensions of Tree 1.

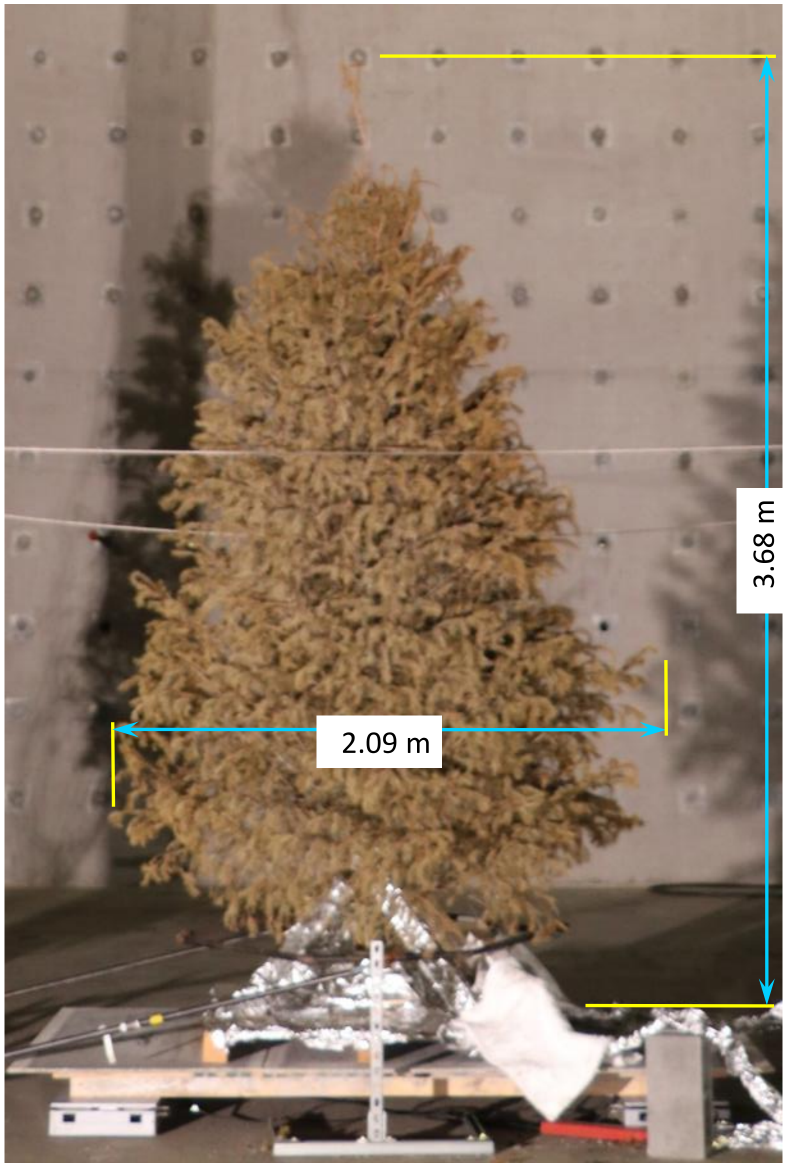

Figure A 2. Test 2 photo with dimensions of Tree 2.

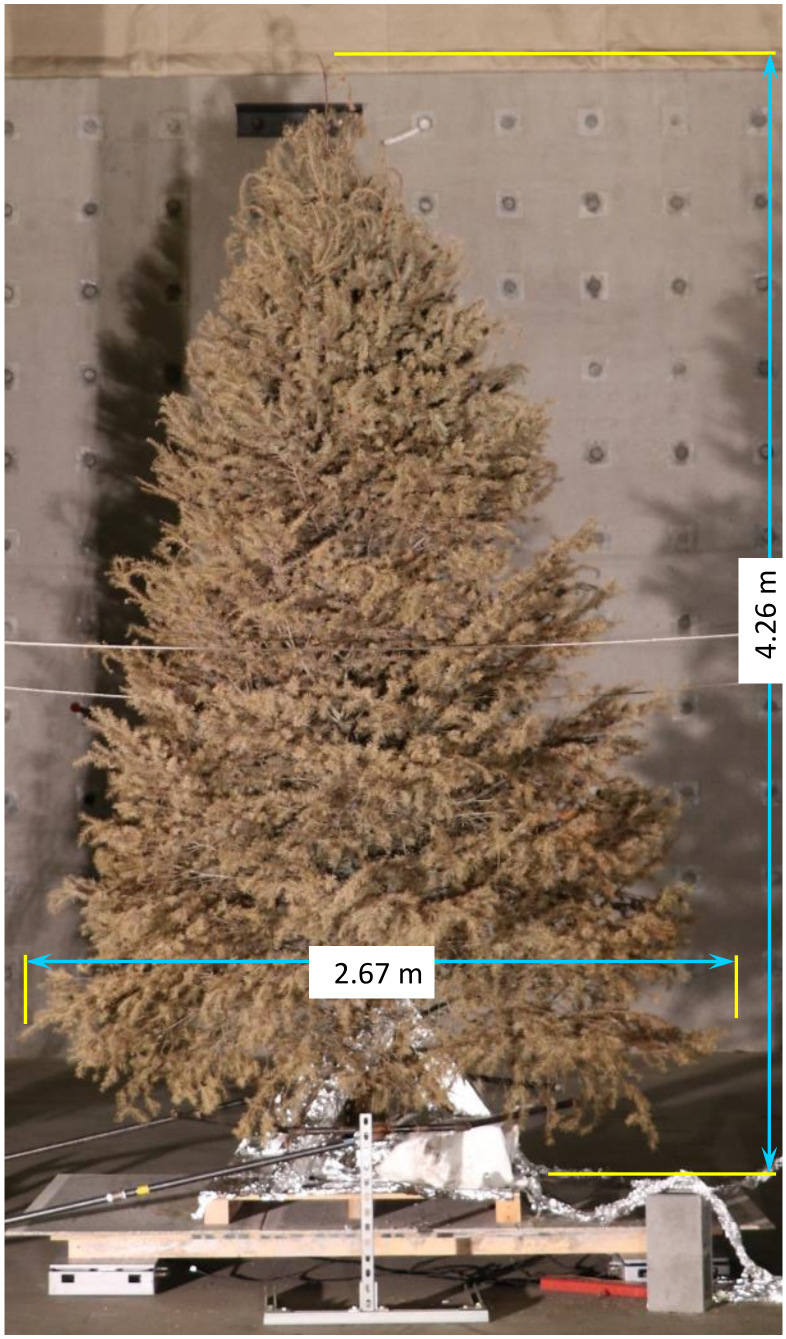

Figure A 3. Test 3 photo with dimensions of Tree 3.

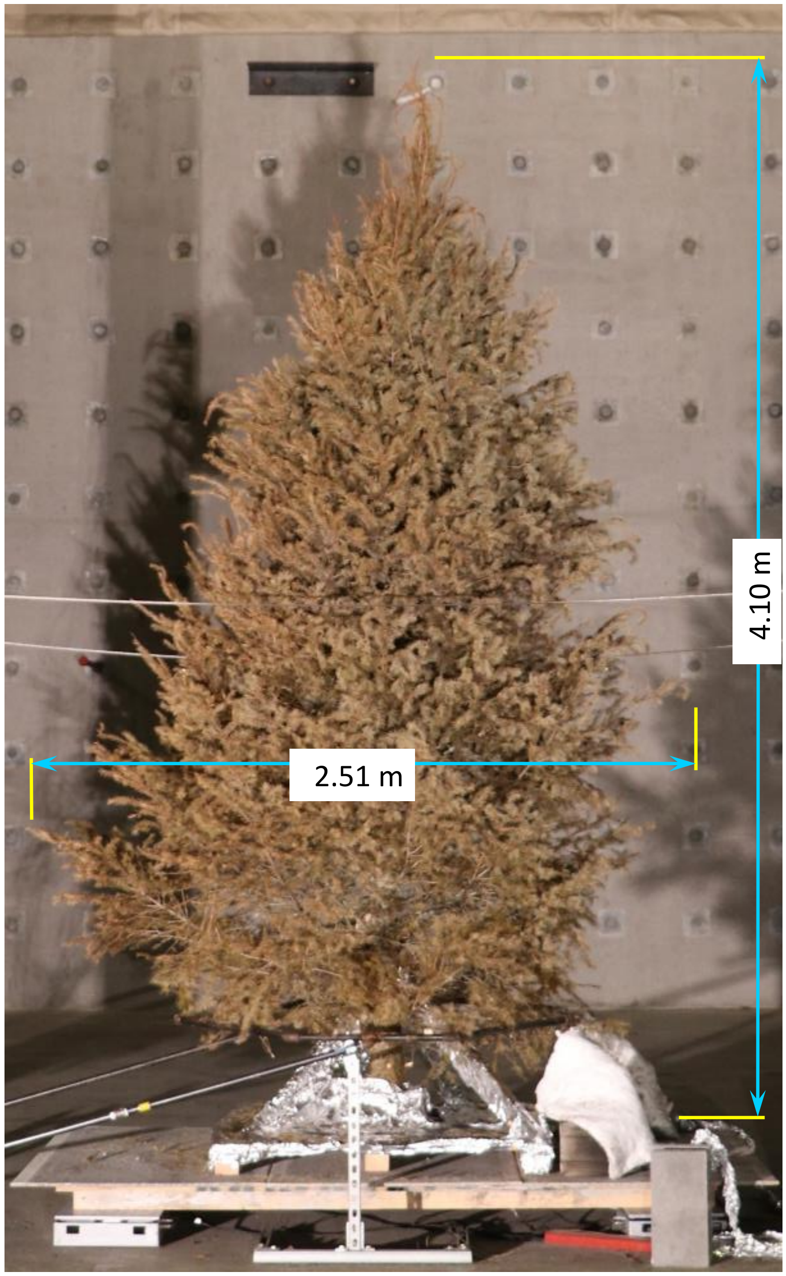

Figure A 4. Test 4 photo with dimensions of Tree 4.

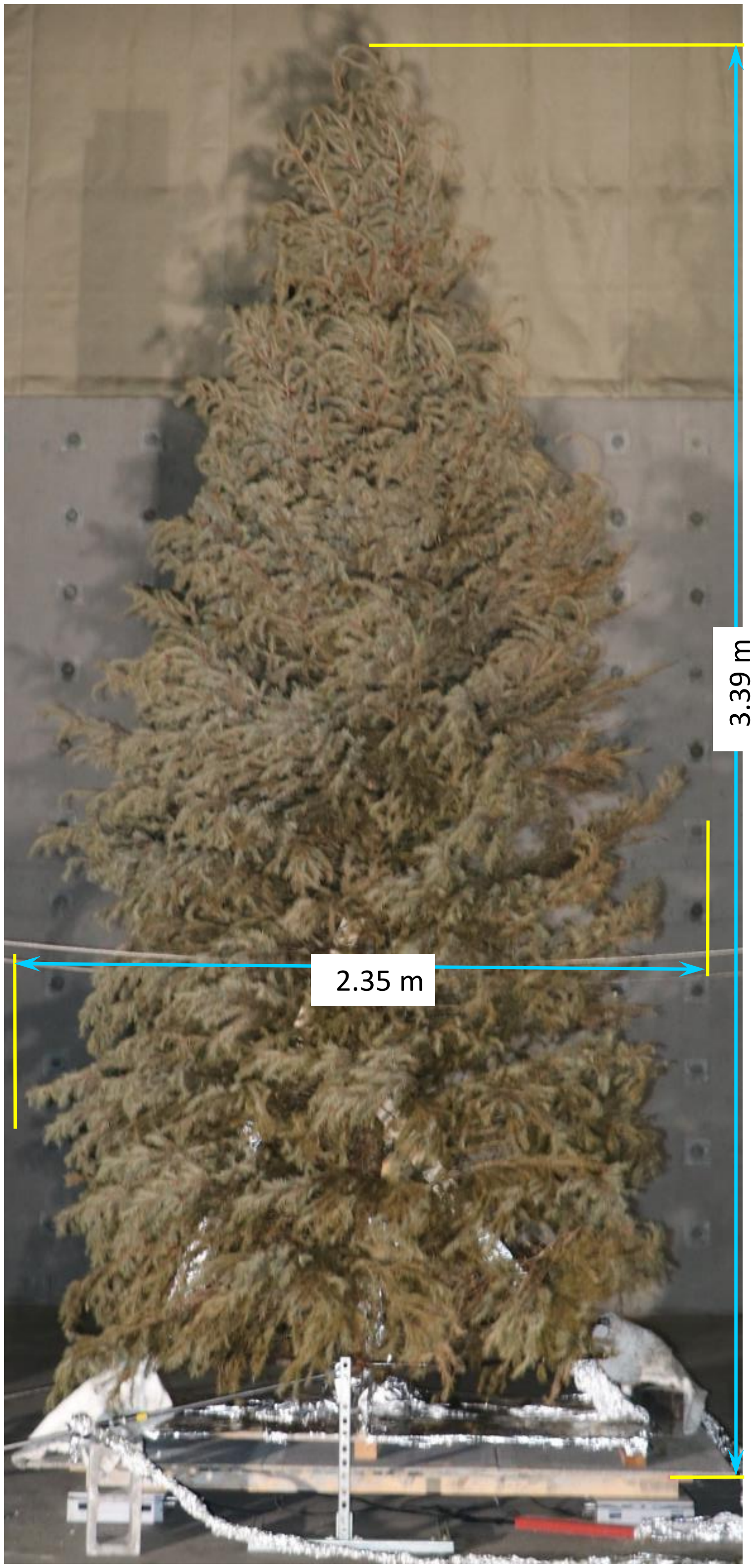

Figure A 5. Test 5 photo with dimensions of Tree 5.

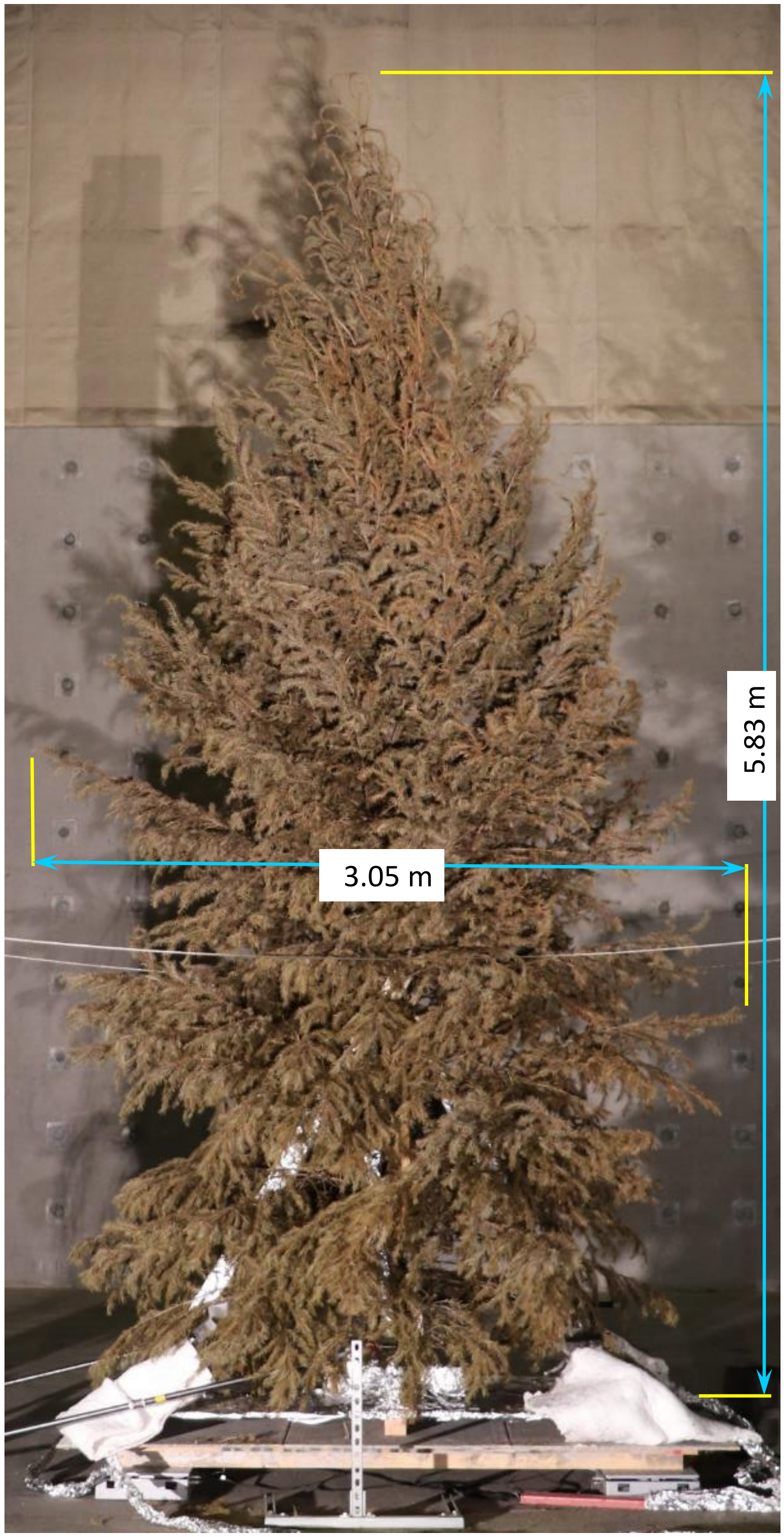

Figure A 6. Test 6 photo with dimensions of Tree 6.

Figure A 7. Tree #1 during the burn and afterward.

Figure A 8. Tree 2 during the burn and afterward.

Figure A 9. Tree 3 during the burn and afterward.

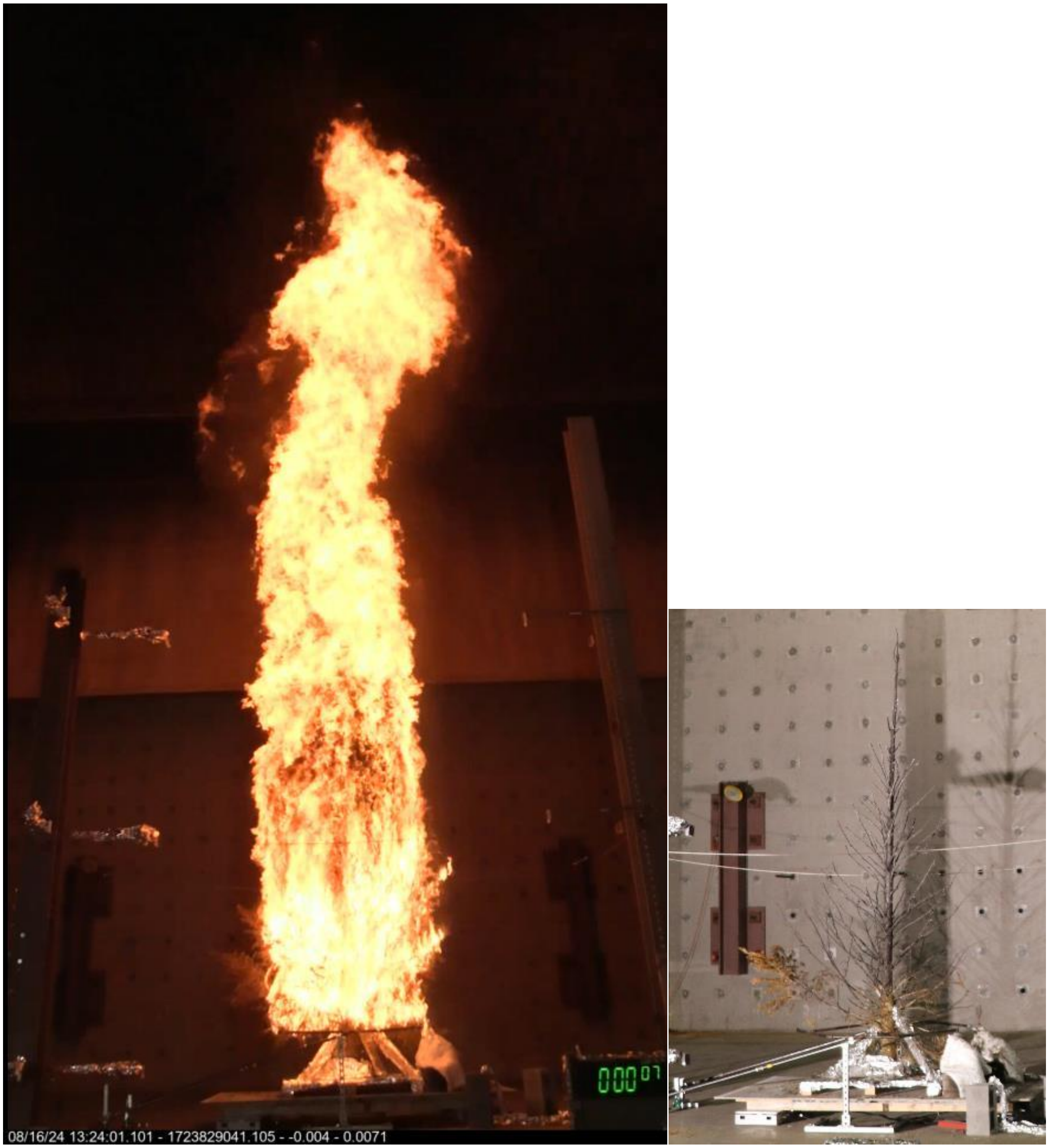

Figure A 10. Tree 4 during the burn and afterward.

Figure A 11. Tree 5 during the burn and afterward.

Figure A 12. Tree 6 during the burn and afterward.

Appendix B. Calorimetry

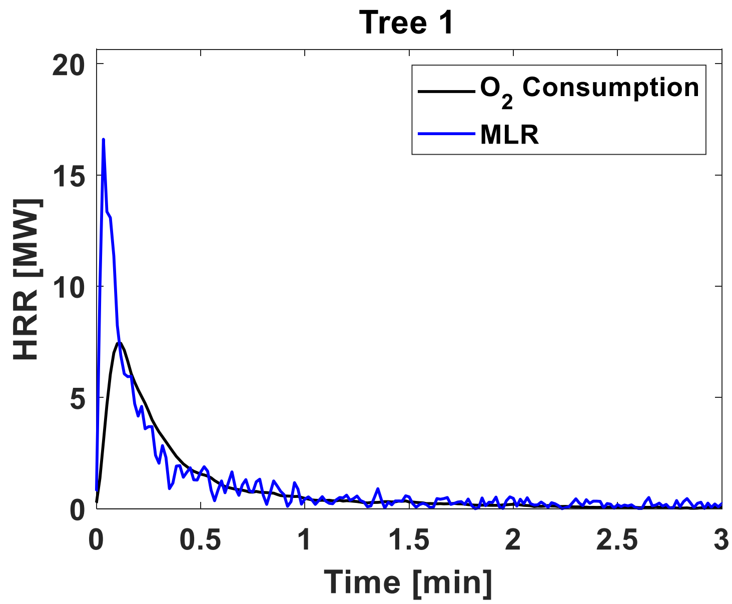

Figure B1. Heat Release Rate measurements using oxygen consumption calorimetry (in black), and mass loss rate (MLR) calorimetry (in blue) of Tree 1. The MLR trace is based on the measured transient mass loss profile and differs from the corrected profile presented in Appendix E (see discussion therein).

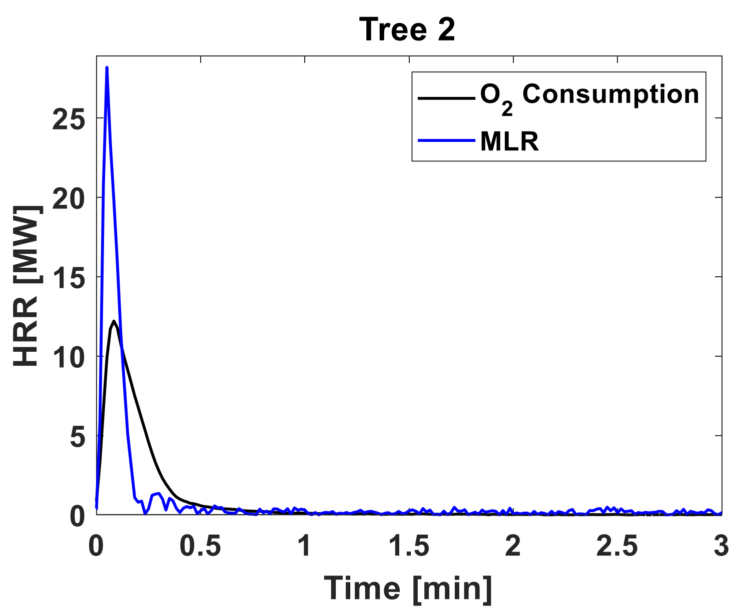

Figure B 2. Heat Release Rate measurements using oxygen consumption calorimetry (in black), and mass loss rate (MLR) calorimetry (in blue) of Tree 2. The MLR trace is based on the measured transient mass loss profile and differs from the corrected profile presented in Appendix E (see discussion therein).

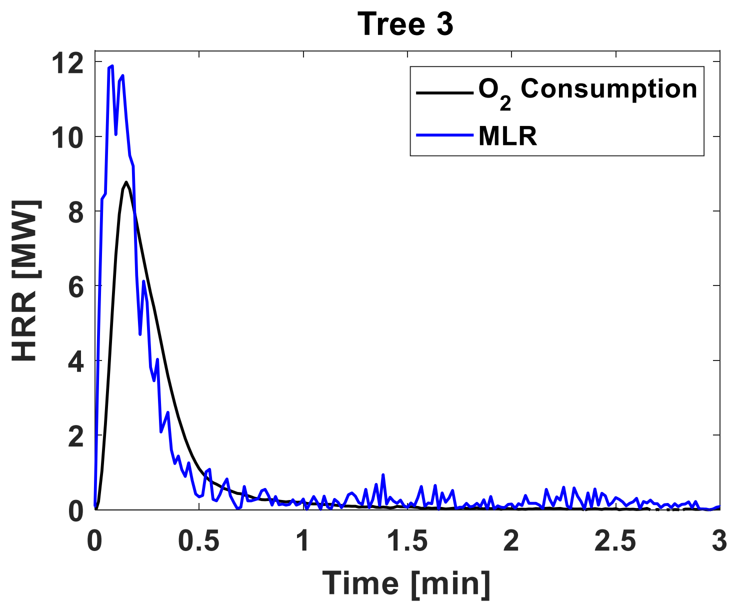

0

Figure B 3. Heat Release Rate measurements using oxygen consumption calorimetry (in black), and mass loss rate (MLR) calorimetry (in blue) of Tree 3. The MLR trace is based on the measured transient mass loss profile and differs from the corrected profile presented in Appendix E (see discussion therein).

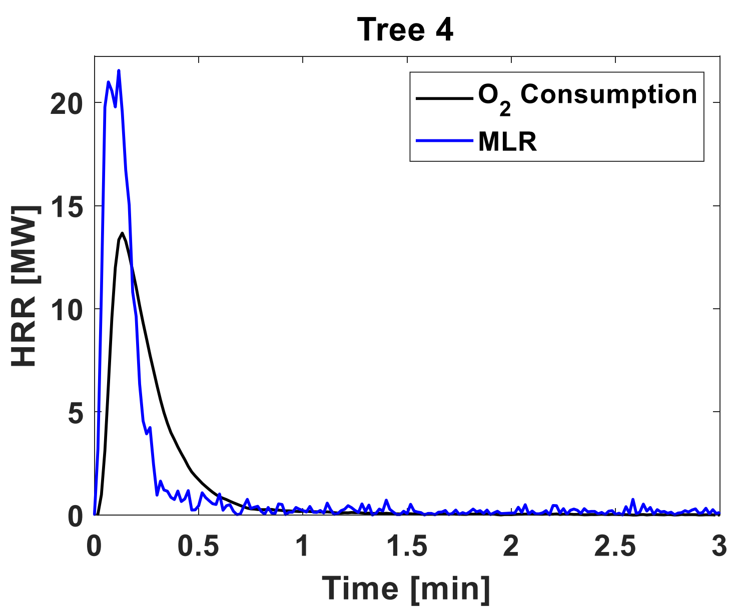

Figure B 4. Heat Release Rate measurements using oxygen consumption calorimetry (in black), and mass loss rate (MLR) calorimetry (in blue) of Tree 4. The MLR trace is based on the measured transient mass loss profile and differs from the corrected profile presented in Appendix E (see discussion therein).

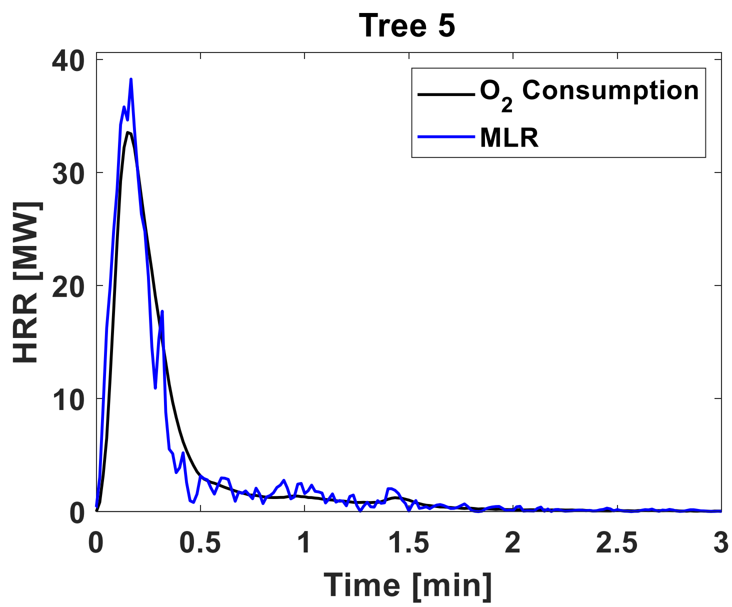

Figure B 5. Heat Release Rate measurements using oxygen consumption calorimetry (in black), and mass loss rate (MLR) calorimetry (in blue) of Tree 5. The MLR trace is based on the measured transient mass loss profile and differs from the corrected profile presented in Appendix E (see discussion therein).

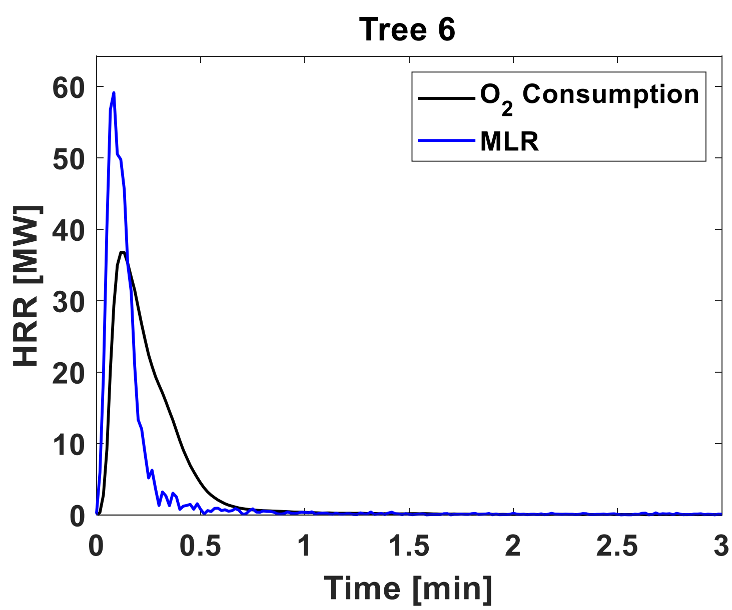

Figure B 6. Heat Release Rate measurements using oxygen consumption calorimetry (in black), and mass loss rate (MLR) calorimetry (in blue) of Tree 6. The MLR trace is based on the measured transient mass loss profile and differs from the corrected profile presented in Appendix E (see discussion therein).

Appendix C. Mass Loss

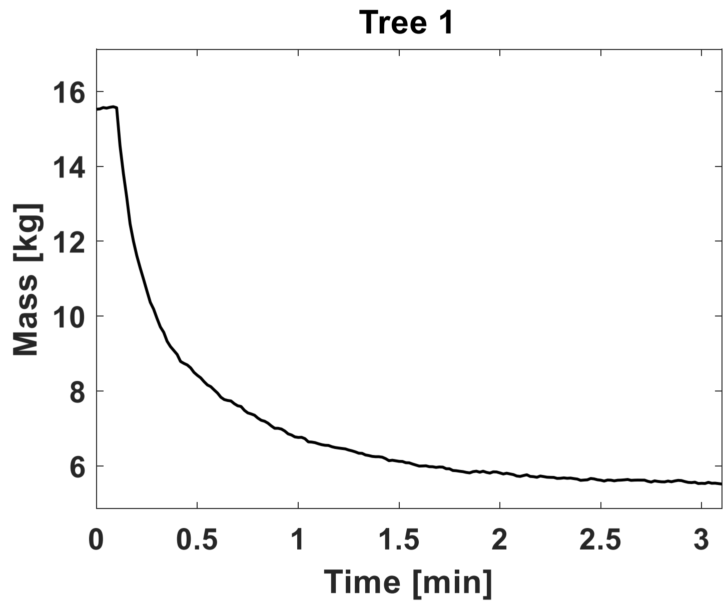

Figure C 1. Tree 1 transient load cell (wet) mass measurements with ignition at time zero.

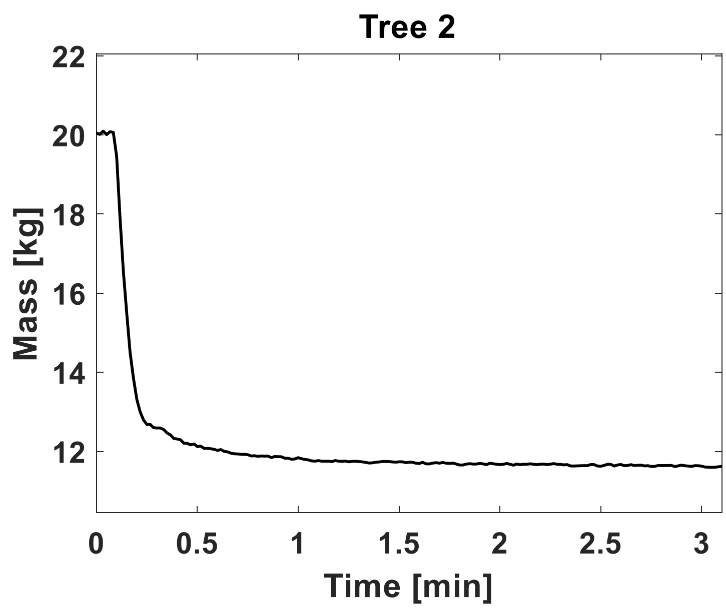

Figure C 2. Tree 2 transient load cell (wet) mass measurements with ignition at time zero.

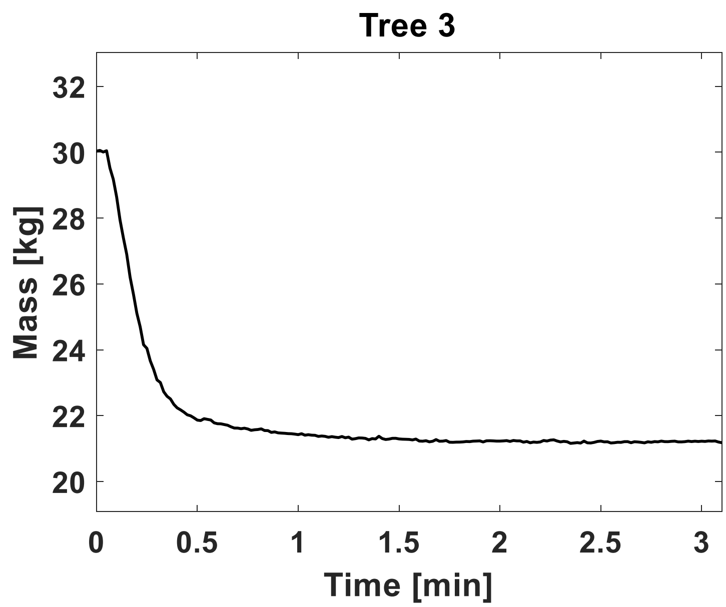

Figure C 3. Tree 3 transient load cell (wet) mass measurements with ignition at time zero.

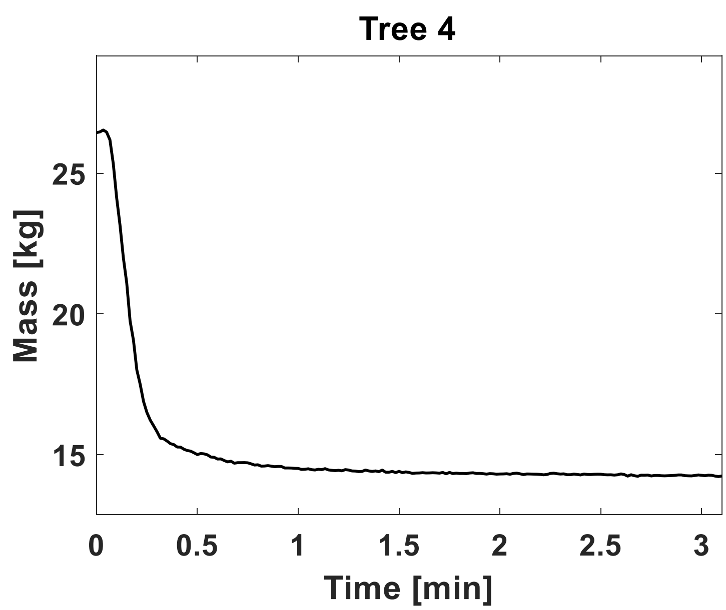

Figure C 4. Tree 4 transient load cell (wet) mass measurements with ignition at time zero.

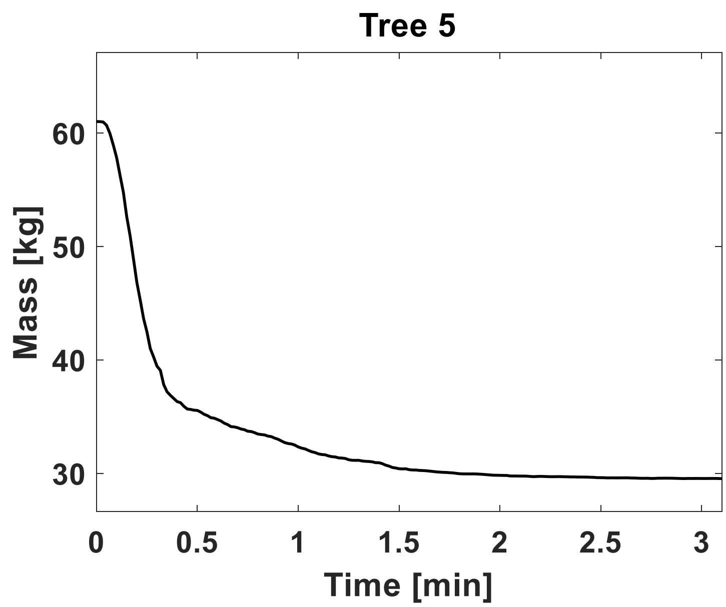

Figure C 5. Tree 5 transient load cell (wet) mass measurements with ignition at time zero.

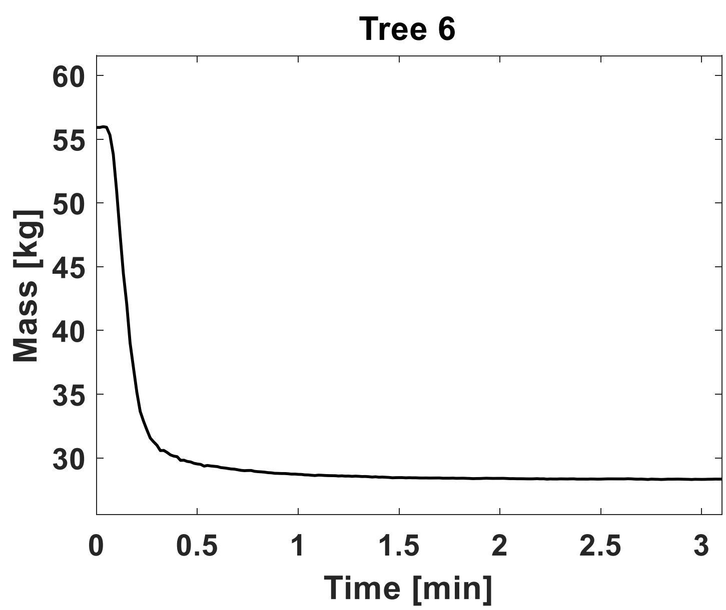

Figure C 6. Tree 6 transient load cell (wet) mass measurements with ignition at time zero.

Appendix D. Heat Flux

D.1. Heat Flux Gauge and Plate Thermometer Comparisons

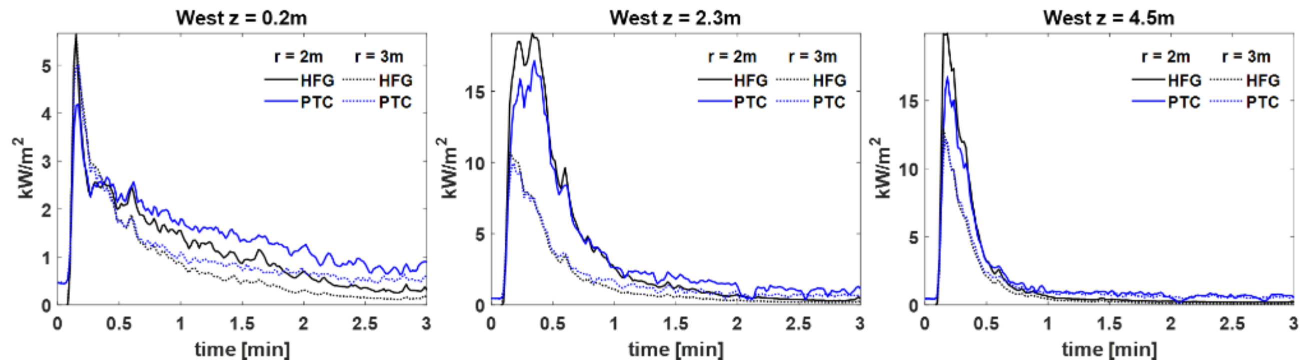

Figure D 1. Tree 1 heat flux gauge and plate thermometer comparison.

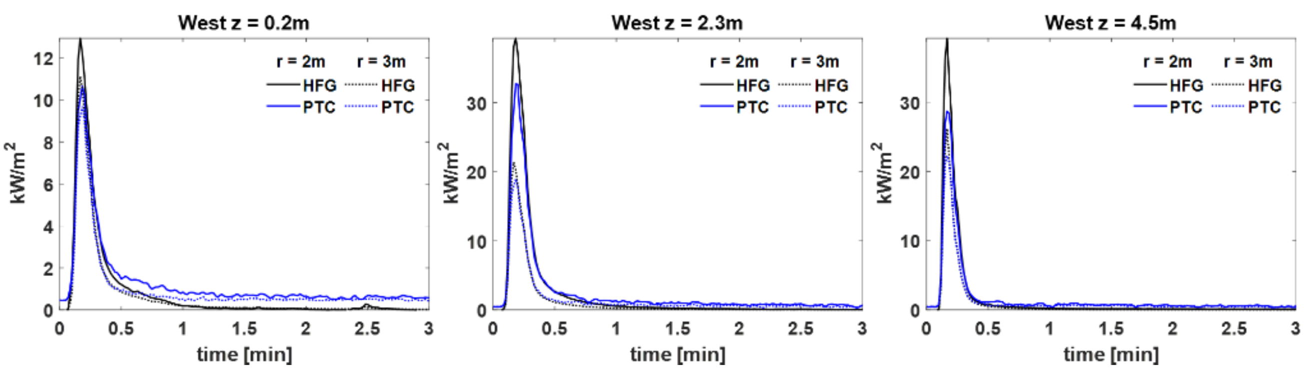

Figure D 2. Tree 2 heat flux gauge and plate thermometer comparison.

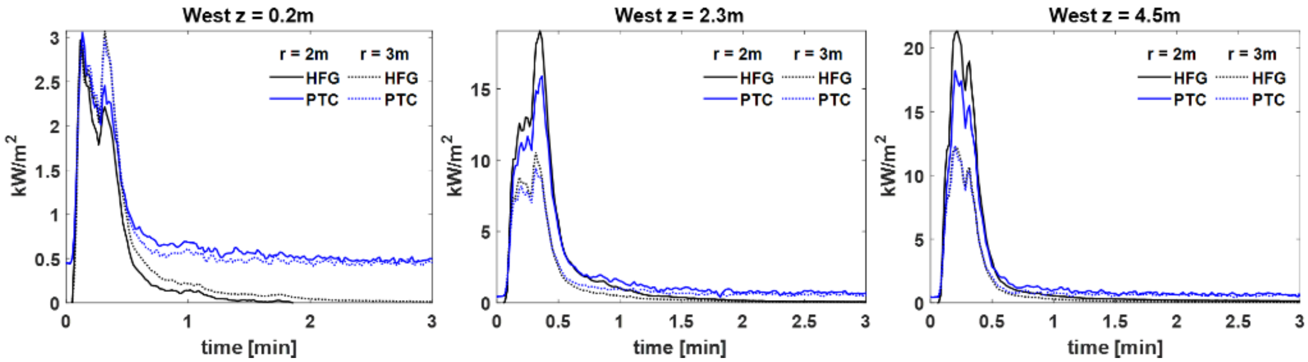

Figure D 3. Tree 3 heat flux gauge and plate thermometer comparison.

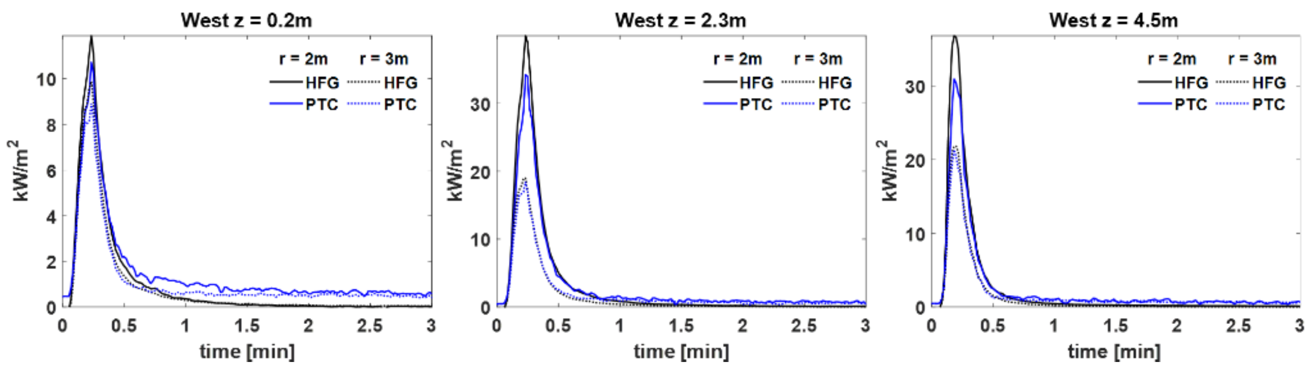

Figure D 4. Tree 4 heat flux gauge and plate thermometer comparison.

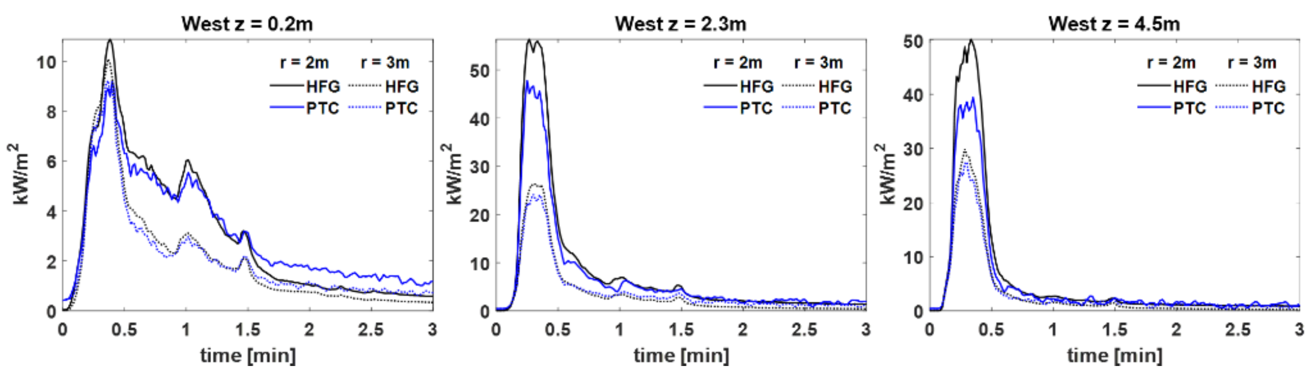

Figure D 5. Tree 5 heat flux gauge and plate thermometer comparison.

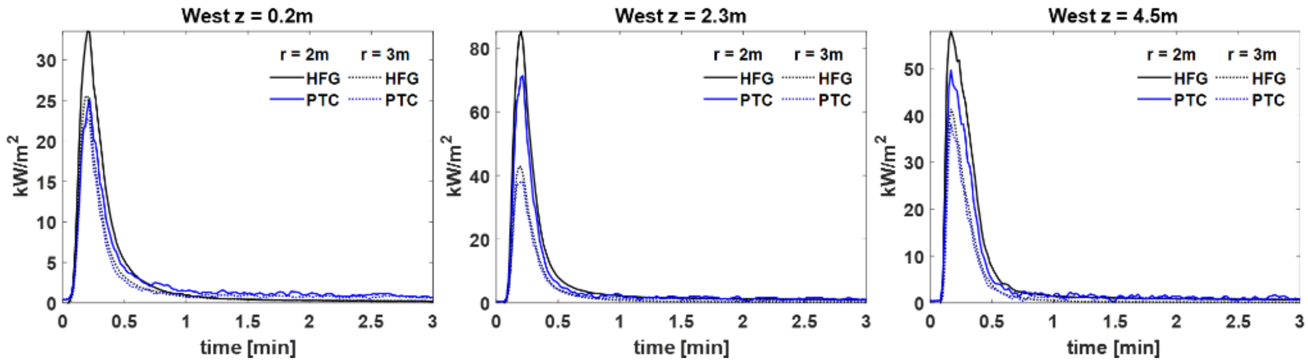

Figure D 6. Tree 6 heat flux gauge and plate thermometer comparison.

D.2. East and West Plate Thermometer Comparisons

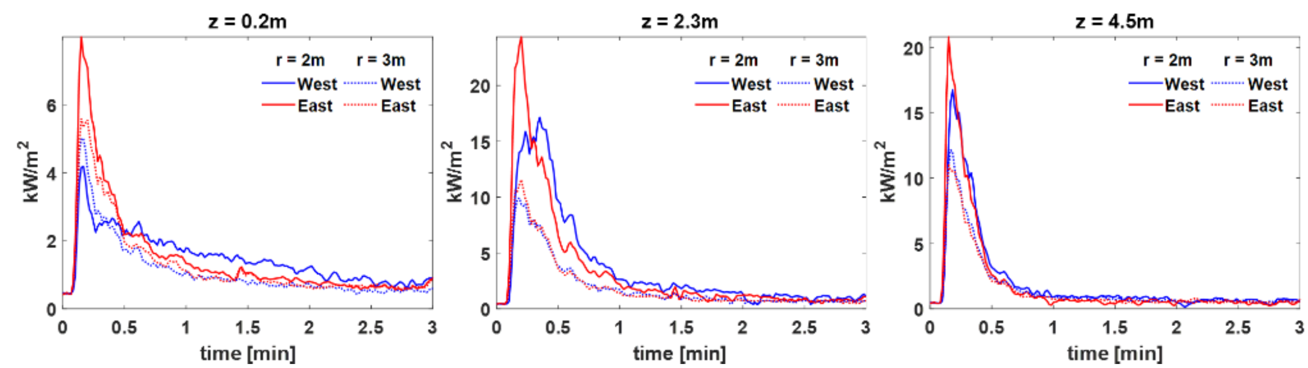

Figure D 7. Tree 1 east and west PT comparisons.

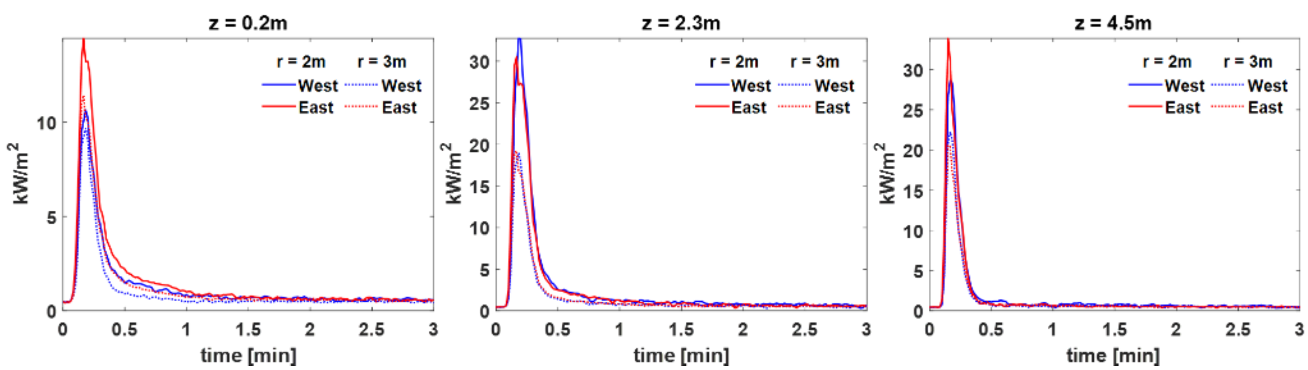

Figure D 8. Tree 2 east and west PT comparisons.

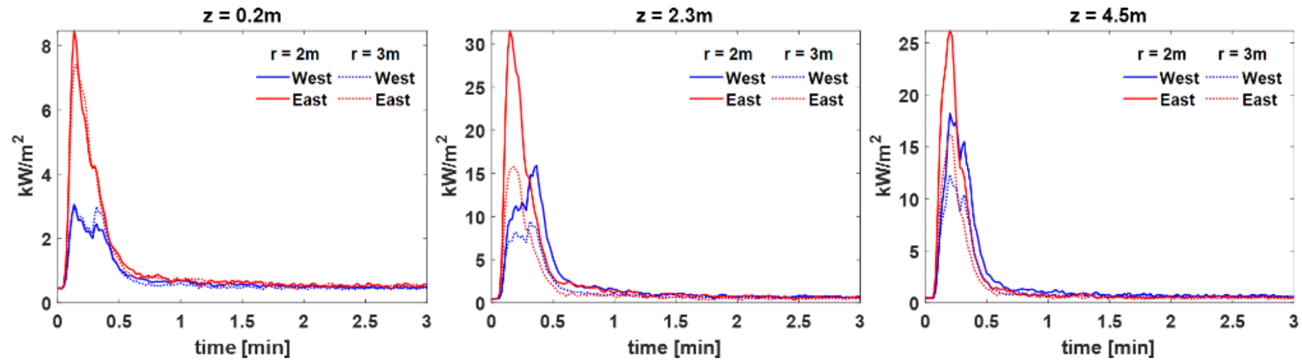

Figure D 9. Tree 3 east and west PT comparisons.

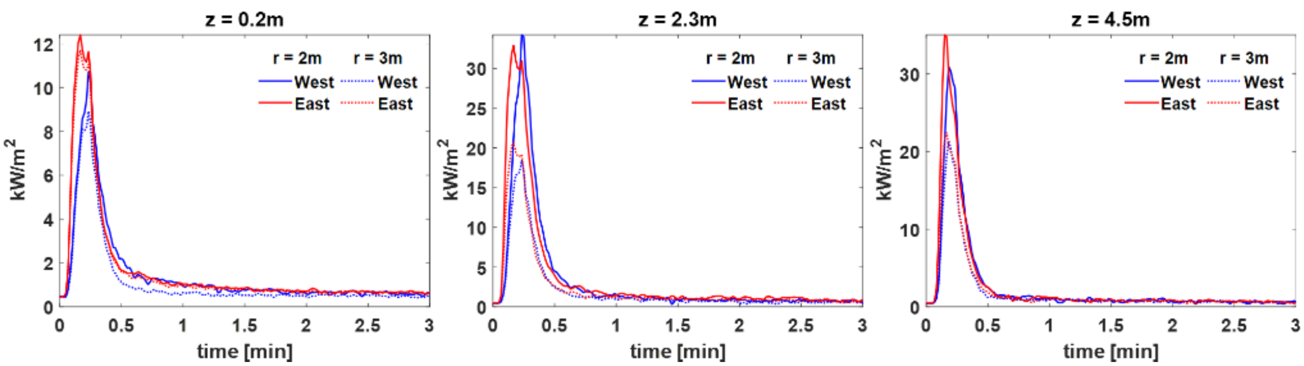

Figure D 10. Tree 4 east and west PT comparisons.

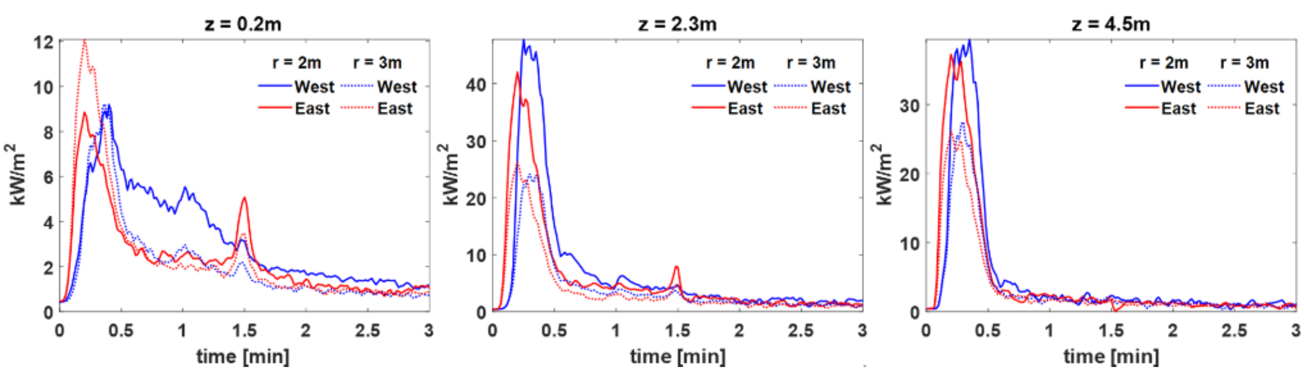

Figure D 11. Tree 5 east and west PT comparisons.

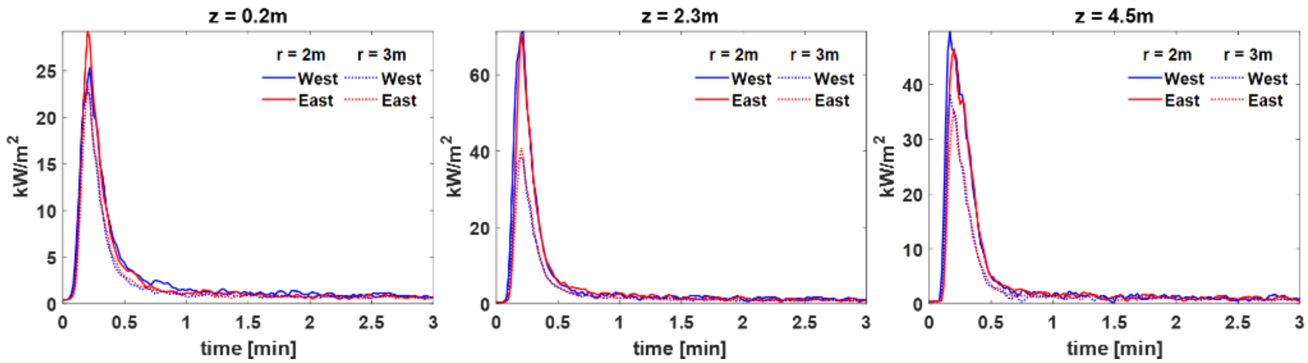

Figure D 12. Tree 6 east and west PT comparisons.

D.3. Far-Field Heat Flux

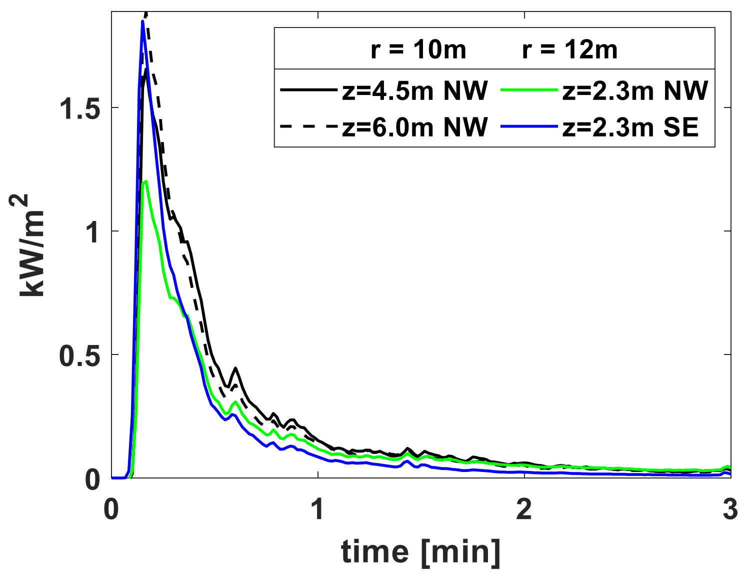

Figure D 13. Tree 1 far-field heat fluxes.

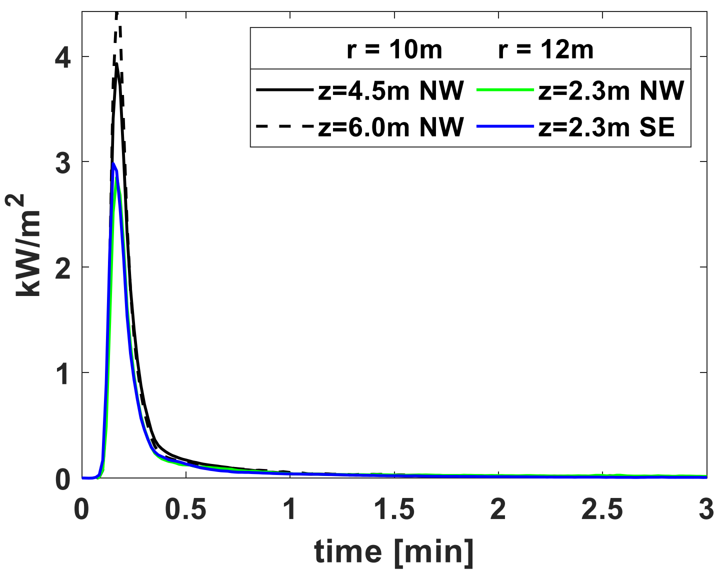

Figure D 14. Tree 2 far-field heat fluxes.

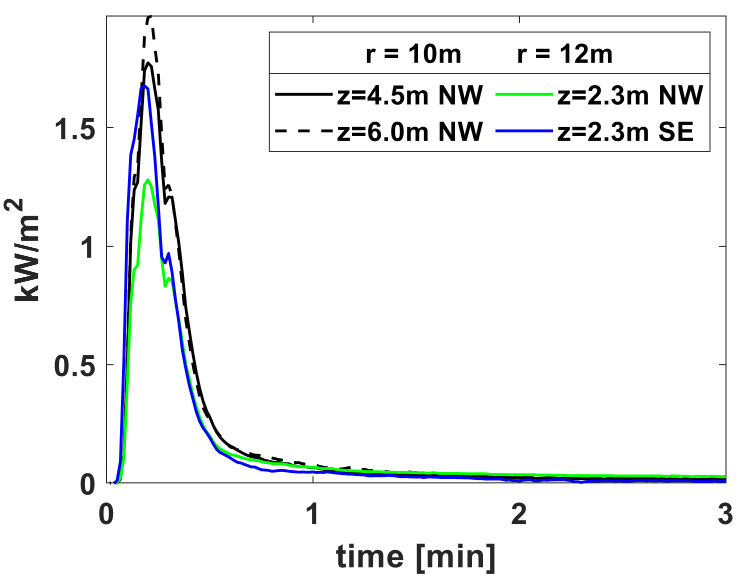

Figure D 15. Tree 3 far-field heat fluxes.

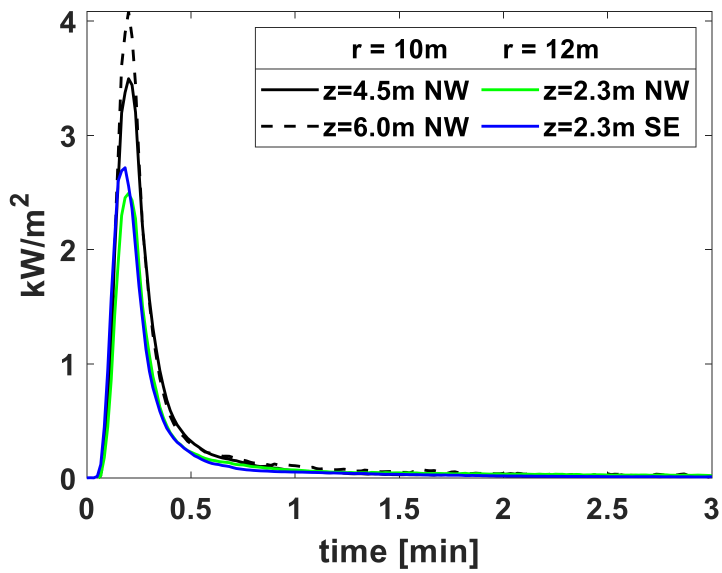

Figure D 16. Tree 4 far-field heat fluxes.

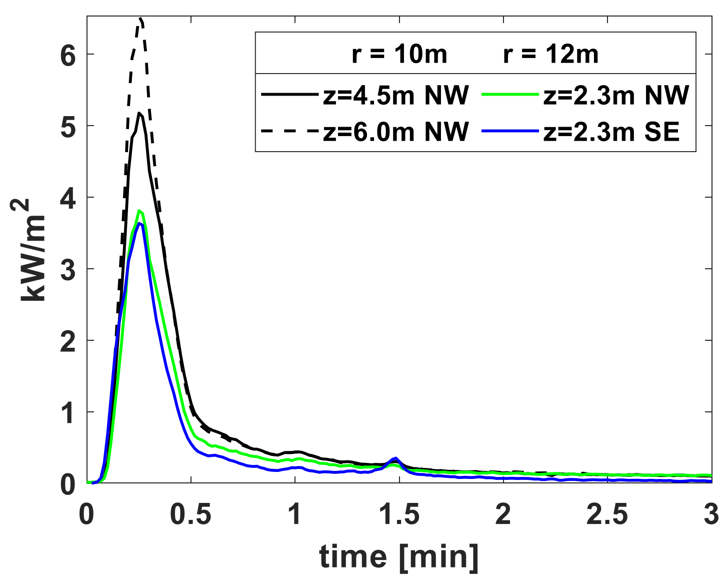

Figure D 17. Tree 5 far-field heat fluxes.

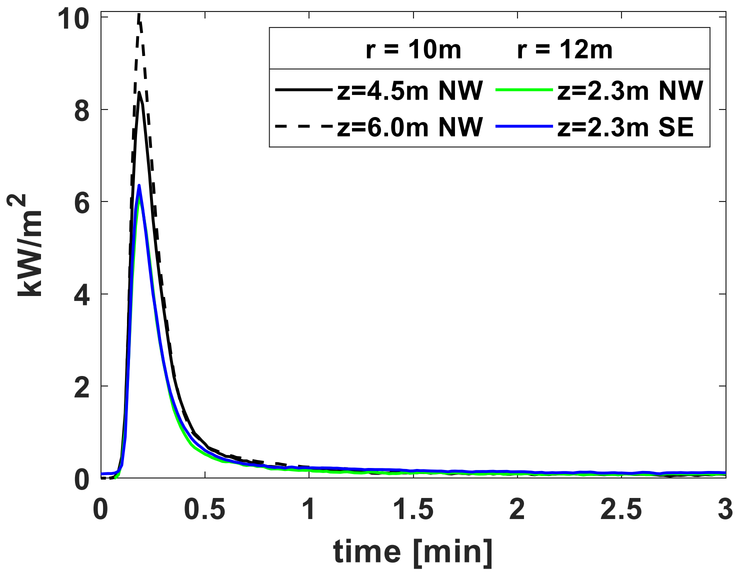

Figure D 18. Tree 6 far-field heat fluxes.

Appendix E. HRR Profiles Corrected for Calorimetry System Time Response

E.1. Background and Approach

Oxygen consumption calorimetry measurements have a system response time that is typically neglected in reported results due to their complex nature [ASTM, 2019 and 2024]. The calorimetry system response time is a convolution of the individual instrument response times (gas concentrations, temperatures, pressure, etc.), mixing of the products of combustion in the canopy hood and ductwork, the flow rate of the exhaust system, and the fire size. A measurement system with a relatively long response time leads to lower measured values of a signal's rate of change and consequent peak broadening and decreased signal extremes (maxima, minima, and fluctuations). For practical purposes, the NIST calorimetry system, like most oxygen consumption calorimetry systems, treats instrument response time as an additional delay time added to the lag time of the various system components. [ASTM 2024] This is because the correction for response time is rather complicated, and the argument goes that for relatively fast response times the difference in the results is small. [ASTM 2024]

Calorimetry measurements in a rapidly growing fire are especially challenging. This is also true for fires in which the volumetric generation rate of exhaust gases is on the same order as the exhaust system extraction rate. In such a case, there may be a build-up of exhaust gases in the canopy hood, where gas products will mix, leading to a longer system response time. Such was the case in the fires studied here for which a transient smoke layer below the canopy hood was observed to grow as the fire HRR increased, indicating that some mixing of combustion products occurred. The NIST 20 MW calorimetry system has a system time constant of approximately 8 s based on analysis of imposed square-wave changes to the HRR determined from calibration experiments using a 20 MW pulse of natural gas imposed in a square wave shaped applied thermal load [Bundy and Bryant, 2019]. Considering that the peak HRRs of the fires investigated in this study occurred less than about 10 s after ignition (see Table 8), the system response time becomes a significant source of uncertainty in the transient results.

In contrast to a calorimetry system, the water-cooled heat flux gauges and the mass load cell system used here are relatively fast. The Huskeflex SGB01 thermal heat flux sensors have a time constant of 450 ms [Huskeflex, 2024], which indicates that 89 % of the true signal is recovered at a 1 Hz sampling interval. This is about 20 times faster than the calorimetry system. On the other hand, strain gauge type devices such as the load cell have a very fast time response, typically on the order of a millisecond.

The calorimetric HRR profile can be rescaled based on the transient profiles of the mass loss rate and the heat flux such that the measured total heat released is invariant, using the following equations:

$$HRR_{\dot{q}''}(t) = 4\pi R^2 \, HF(t) \, THR/TRE \tag{E1}$$

$$HRR_{\dot{m}}(t) = MLR(t) \frac{THR}{\int_0^{t_f} MLR(t) \, dt} = MLR(t) \frac{THR}{\Delta m} \tag{E2}$$

where the time varying fuel mass loss rate (*MLR(t)*) corrected for moisture content is determined from the load cell data (see Appendix C) using a central differencing scheme, *TRE* is the average of the total radiated energy in Table 10 (using the NW and SE heat flux gauges), *THR* is the total heat release measured by calorimetry (see Table 8), *HF(t)* is the averaged profile of the measured far field transient heat flux (see Appendix D) at distance *R* from the tree's central axis (R=12 m), t_f is the duration of the fire, and Δm is the total fuel mass burned (see Table 8). The ratio of THR to Δm in Equation E2 is referred to as the net heat of combustion in the NIST Fire Calorimetry Database (FCD).

E.2. Assumptions and Limitations

Rescaling the HRR profile based on the heat flux gauge profile and the total heat release measured by calorimetry assumes that the radiative fraction is constant as a function of time (and implicitly, as a function of HRR) during the fires. It also assumes that smoke and gas absorption does not reduce the measured radiative signal intensity and that the entire fire is visible and unobscured.

Rescaling the HRR profile based on the mass loss rate profile assumes that the drag experienced by the tree does not impact the transient load cell measurement. However, a computational fluid dynamic fire model of the Douglas-fir tree experiments using FDS 6.9.1 [McGrattan, 2024] shows that the drag force can be significant and that it changes with time as the tree burns away and the velocity field changes. The drag force is zero when there is no buoyancy induced flow at the start and end of the fire. As the fire starts, the buoyant plume generated by the fire interacts with the foliage and branches producing a drag force that reduces the mass loss measurement. The drag force increases with the increase in buoyant flow, with estimated peak values on the order of 1 kgf (or 10 N). The force decreases as both the foliage burns away and the induced flow decreases. While the maximum velocity occurs at the time of peak heat release, the maximum foliage surface area is at the start of the test. Thus, the drag may shift the measured mass loss profile and the calculated maximum of the mass loss rate (and peak heat release rate of the rescaled HRR profile). A second assumption regarding rescaling the HRR profile with the mass loss rate profile is that all combustion occurs with the foliage attached to the tree. Of course, this is not true as a significant amount of combustion occurs in the gas phase. In addition, a number of embers were observed during the fires, which detach from the tree and burn while being lofted. A third assumption is that the net heat of combustion is invariant during the burn with a combustion efficiency of 100 %. A fourth assumption is that the percentage moisture content of the tree is invariant during burning. It should also be noted that a central differencing scheme was used to determine the mass loss rate (MLR) profile from the measured time varying mass, which adds a 2 s response time to the corrected HRR profile.

There are differences in the measured values of Δm and $\int_0^{t_f} MLR(t)\,dt$ in Equation E2 equal to 10 % on average. As previously described, both measurements use the same load cell system (which was calibrated). The former quantity represents measurements made at time zero and at the end of the fire test when the loads were static. The latter quantity represents integration of the time varying load cell data, which is subject to the dynamics of the experiments and the assumptions and limitations outlined above including the effects of time varying drag. In this study, the more-straightforward static measurement was used when evaluating Δm in Equation E2.[3]

Accurately accounting for all the assumptions and limitations outlined in this subsection is impossible, exacerbated by the relatively large measurement and modeling uncertainties. Thus, both rescaling methods (Equations E1 and E2) are imperfect Yet, a first pass at correcting the calorimetric HRR profile offers insight on the character of the rapidly growing tree fires as discussed below.

E.3. Results

Figure E1 to Figure E6 show the rescaled HRR profiles using Equations E1 and E2 compared to the HRR profiles based on oxygen consumption calorimetry and the mass loss rate times the net heat of combustion (denoted as MLR in the figures). As expected, the rescaled profiles generally have narrower peaks that are larger in magnitude than the peaks measured by oxygen consumption calorimetry. Table E1 summarizes the results, presenting the values of the peak HRRs and times to peak HRR measured by oxygen consumption calorimetry ($\boldsymbol{HRR_{O_2}}$), the mass loss rate times the heat of combustion ($\boldsymbol{HRR_{MLR}}$**;** Equation 7), and the rescaled HRR profiles using the mass loss

[3] To ensure that the second equality in Equation E2 holds, the *MLR(t)* data traces were corrected, multiplying each trace by a scaling factor (0.8, 0.79,0.76, 0.85, 0.96, 0.95 for Trees 1 -6, respectively). Note that the corrected mass loss profiles with these scaling factors differ from the plots shown in Figure B1 to Figure B 6 due to unaccounted biases in the load cell mass loss measurements associated with buoyancy induced drag and possibly other factors.

rate ($HRR_{\dot{m}}$; Equation E2) and the far-field heat flux ($HRR_{\dot{q}''}$; Equation E1) profiles. The largest peak HRR values and the fastest times to the peak HRRs in Table E1 are associated with the ***HRR_{MLR}*** and $HRR_{\dot{m}}$ profiles, which are both based on the mass loss rate profiles. These two HRR profiles have the same overall shape, the difference attributed to the fact that the integral of the HRR_{MLR} profile is not constrained to equal THR whereas the $HRR_{\dot{m}}$ profile is constrained in this manner. So, these two profiles are essentially scaled by different constants. To determine the ratio of the constants, consider the ratio of the two profiles defined in Equations 7 and E1, which yields:

$$\frac{HRR_{MLR}(t)}{HRR_{\dot{m}}(t)} = \frac{\mathrm{MLR\ (t)}\ H_{c,net}}{MLR(t)\frac{THR}{\Delta m}} = \Delta m\ H_{c,net}/THR \tag{E3}$$

Since the curves have identical shapes, Equation E3 also represents the ratio of the profiles at the times of the peak HRR (which of course are identical). Considering each of the trees in Table E1, the values of the peaks of the HRR_{MLR} and $HRR_{\dot{m}}$ profiles are within 17 % of each other for all tests and differ by 9 % on-average.

Table E1. The values and expanded combined expanded (k=2) uncertainties of the peak HRR and times to peak HRR measured by oxygen consumption calorimetry (HRR_{O_2}), the fuel mass loss rate times the heat of combustion (HRR_{MLR}; Equation 7), and the rescaled HRR profiles using the mass loss rate ($HRR_{\dot{m}}$; Equation E2) and the far-field heat flux ($HRR_{\dot{q}''}$; Equation E1) profiles.

	HRR_{O_2}		HRR_{MLR}		$HRR_{\dot{m}}$		$HRR_{\dot{q}''}$	
Test	Peak HRR [MW]	Time to Peak [s]	Peak HRR [MW]	Time to Peak [s]	Peak HRR [MW]	Time to Peak [s]	Peak HRR [MW]	Time to Peak [s]
1	7.4±0.8	7±4	17.1± 12.5	2 ± 2	11.7 ± 8.6	2 ± 2	9.7 ± 3.3	4 ± 2
2	12.2±1.3	5±4	28.2± 20.7	3 ± 2	21.7 ± 14.4	3 ± 2	20.4 ± 3.2	6 ± 2
3	8.8±0.9	9±4	11.9± 8.6	5 ± 2	8.1 ± 4.8	5 ± 2	9.9 ± 2.8	10 ± 2
4	13.7±1.4	8±4	21.6±15.7	7 ± 2	16.9 ± 10.3	7 ± 2	17.7 ± 3.0	9 ± 2
5	33.5 ±3.6	9±4	38.3±27.8	10 ± 2	36.4 ± 12.6	10 ± 2	31.4 ± 4.8	14 ± 2
6	36.8 ±3.9	7±4	59.1± 43.1	5 ± 2	67.3 ± 26.5	5 ± 2	54.1 ± 8.3	9 ± 2

The uncertainties associated with the rescaled HRR peaks in Table E1 (and the profiles themselves) are relatively large. The (combined expanded, k=2) uncertainty in the peak HRR rescaled by the heat flux profile ($HRR_{\dot{q}''}$) is related to the relative uncertainties in the THR (6 % on average; see Table 8) and TRE (14 % on average; see Section 3.4), as well as the range of results associated with averaging the far-field heat flux measurements (12 % on average). The (combined expanded, k=2) uncertainty in the peak HRR rescaled by the MLR profile ($HRR_{\dot{m}}$) is related to the uncertainties in the THR and the total mass loss measurement (24 % on average; see Table 8), as well as the estimated errors in the central differencing scheme (43 % on average), which dominates the relative uncertainty. This dominant term can be attributed to the relatively slow data sampling rate (1 Hz) compared to the relatively rapid change in the mass loss rate, and that the uncertainty in the central difference scheme is proportional to the square of the time step of the data and truncation error of the Taylor series. The uncertainty in the $\boldsymbol{HRR_{MLR}}$ profile is about as large as that of the $\boldsymbol{HRR_{\dot{m}}}$ due to the contributions to uncertainty associated with the moisture content, the net heat of combustion, and the central differencing scheme.

In summary, the analysis shows that for relatively fast growing fires, use of fast time response instrumentation can supplement oxygen consumption calorimetry, providing a means to rescale the HRR profile. In this study, rescaling the HRR using the heat flux gauge signals led to peaks that were smaller than rescaling using the mass load cell measurement. In hindsight, much of the uncertainty in both mass-based profiles ($\boldsymbol{HRR_{MLR}}$ and $\boldsymbol{HRR_{\dot{m}}}$) would have been reduced if the data acquisition rate had been increased by an order of magnitude for the rapidly growing tree fires investigated in this study.

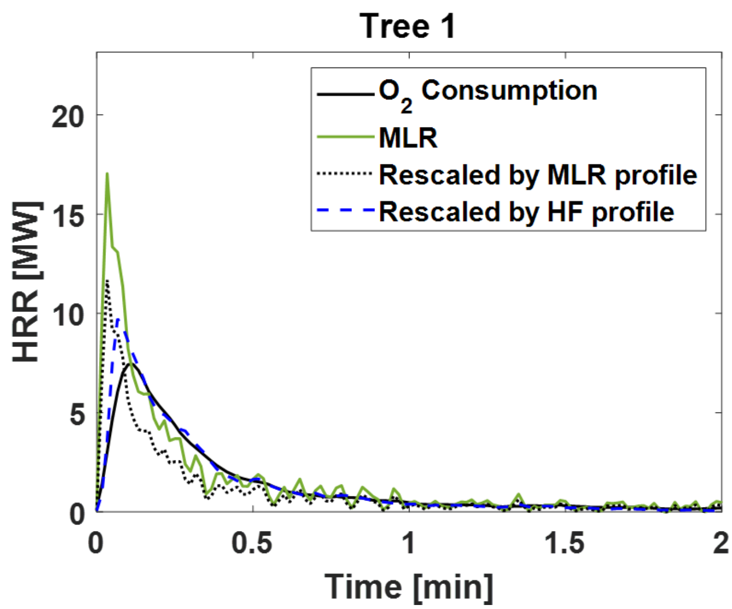

Figure E1. Rescaled transient HRR profiles compared to the Oxygen and MLR calorimetry results for Tree 1.

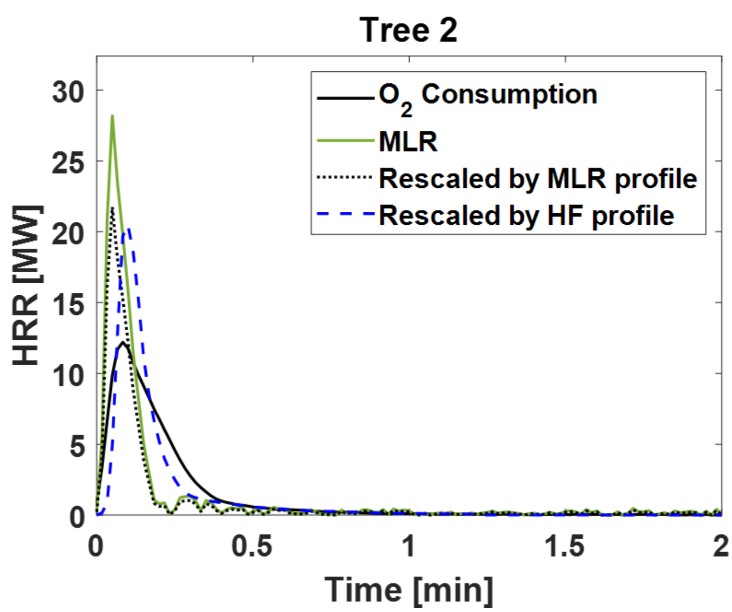

Figure E2. Rescaled transient HRR profiles compared to the Oxygen and MLR calorimetry results for Tree 2.

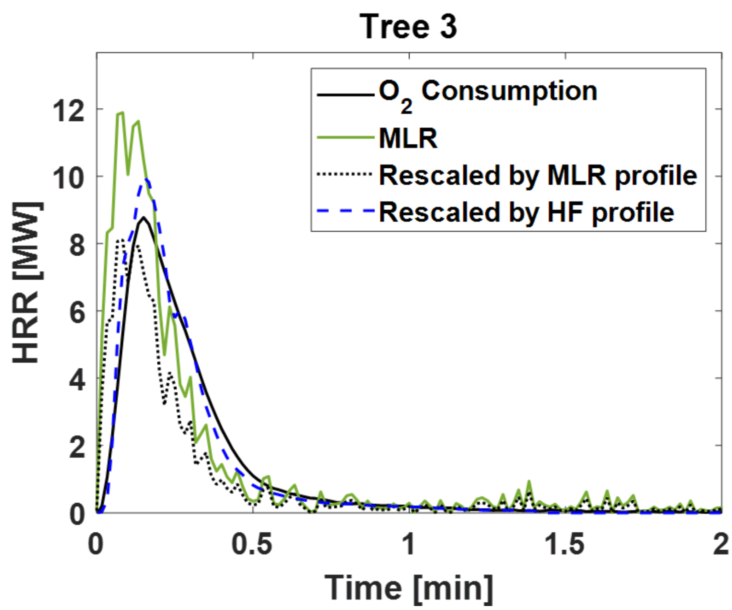

Figure E3. Rescaled transient HRR profiles compared to the Oxygen and MLR calorimetry results for Tree 3.

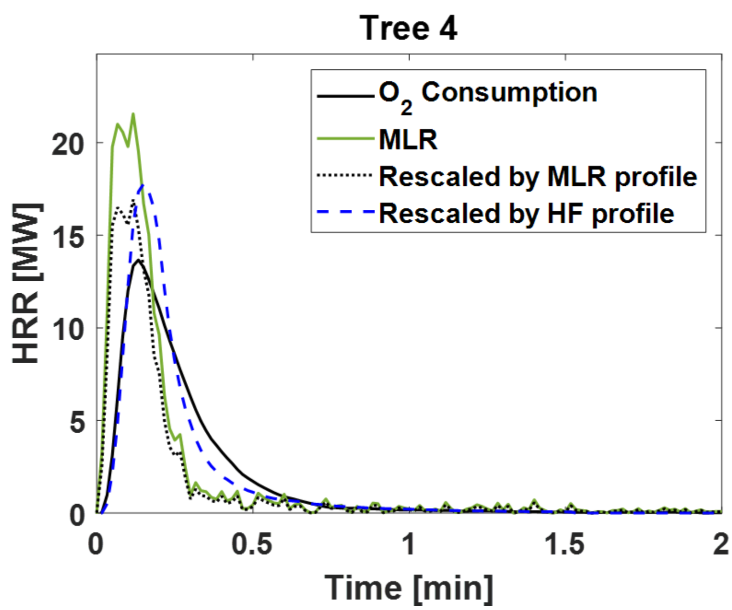

Figure E4. Rescaled transient HRR profiles compared to the Oxygen and MLR calorimetry results for Tree 4.

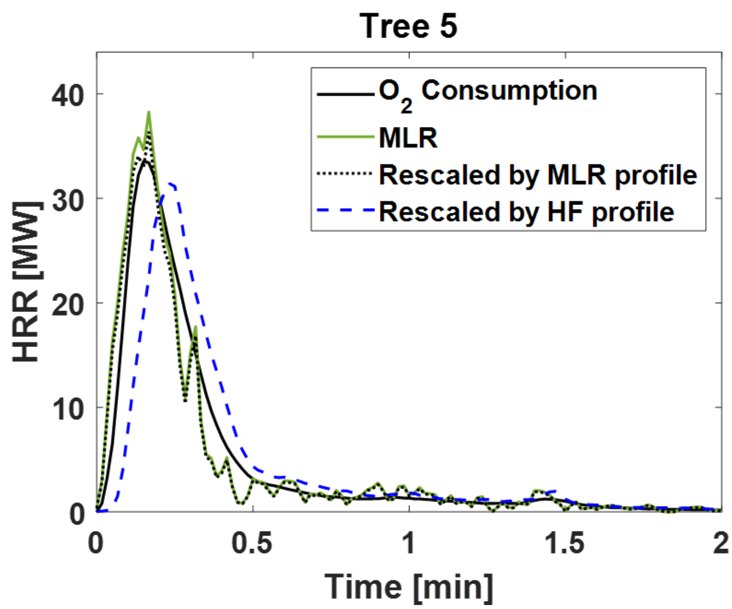

Figure E5. Rescaled transient HRR profiles compared to the Oxygen and MLR calorimetry results for Tree 5.

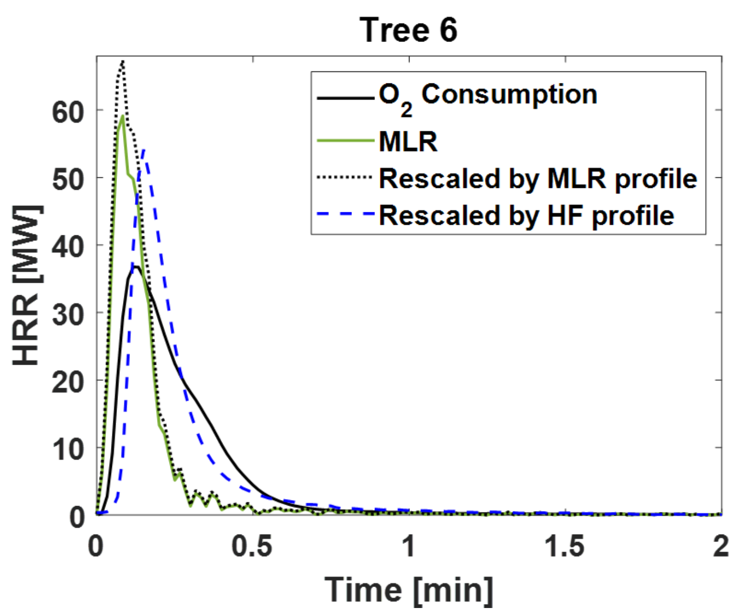

Figure E6. Rescaled transient HRR profiles compared to the Oxygen and MLR calorimetry results for Tree 6.

Appendix F. Uncertainty in Photogrammetry Measurements

This section provides an estimate of the uncertainty associated with geometry measurements derived from photogrammetry. The proprietary algorithm does not have any stated accuracy, so instead, a point cloud was created from a known object using the same technique applied to the trees. In this case, one of the instrumentation support columns was used, with specific focus on two reference lengths: (1) the width of the column from the outside of the flanges, and (2) the width of the base plate. The photogrammetric model and the two references lengths are shown in Figure F1.

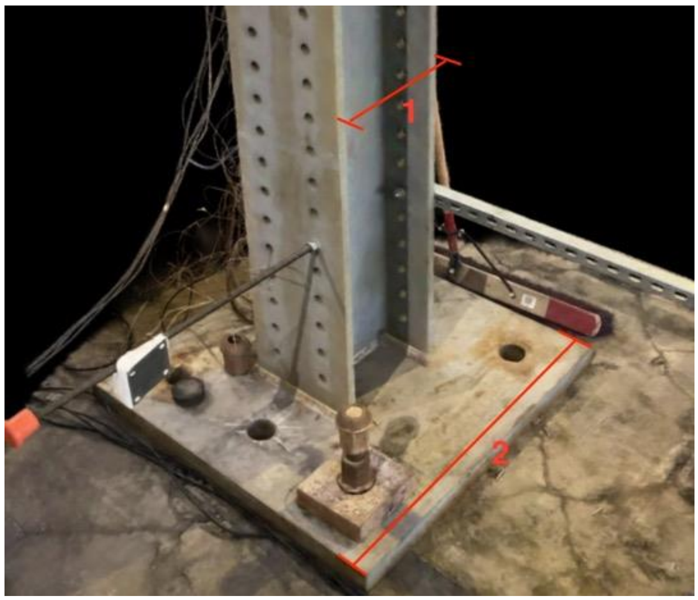

Figure F1. Photogrammetric model of reference object (east column in Figure 2).

Points were extracted that were associated with the outside of the flanges over a 20 cm vertical length and 20 cm depth and associated with the edges of the base plate over a 20 cm depth. The reference edges were oriented in the x-direction and the average x-location of the relevant points was used to define the reference length, as shown in Figure F2.

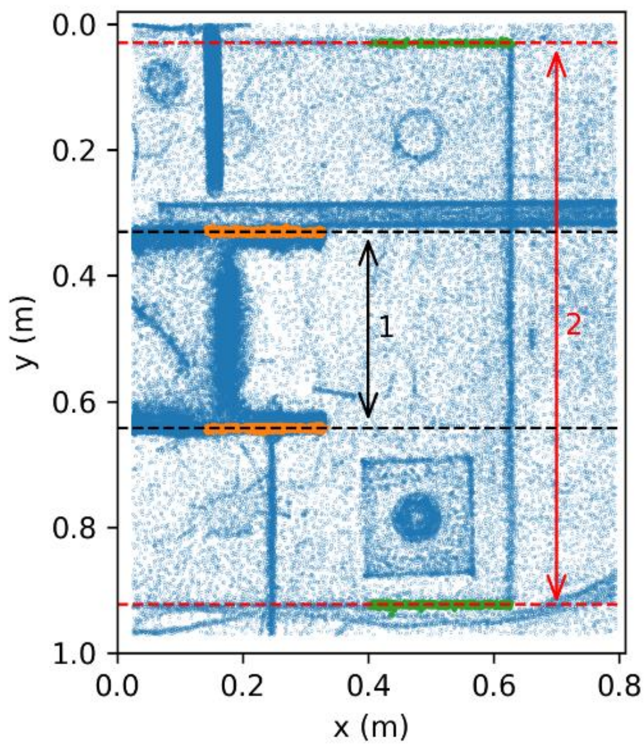

Figure F2. Raw point cloud from photogrammetric model in previous figure. The points corresponding to the reference measurements are highlighted in orange (reference length 1) and green (reference length 2). The calculated model distances are shown as dashed lines.

The uncertainty shown in **Error! Reference source not found.** is considered a conservative e stimate because the orientation of the scene and the determination of points associated with reference edges was performed by hand. This conservative approach is followed yielding an uncertainty of a point location as 2 cm.

Table F 1: Type A uncertainty in point cloud location based on measurement of reference distances.

Reference Length	Actual Length (cm)	Average Point Cloud Distance (cm)	Uncertainty (cm)	Relative Uncertainty (%)
1	32.8	31.3	1.5	4.6
2	91.4	89.4	2.0	2.2

The absolute uncertainties for point locations are smaller than the dimensions used in the voxelization process, thus a significant contribution to uncertainty of voxel-based measurements is assumed to come from the voxel sizes (Δx) themselves. Linear measurements are assumed to have a combined expanded uncertainty (coverage factor $k = 2$) of:

$$U_{dist} = 2\sqrt{\Delta x^2 + (0.02)^2}$$

The uncertainty of the volume is more complicated to quantify due to the irregular nature of the voxelized geometry. However, a rough estimate can be derived from assuming an elliptical conical volume from the three linear dimensions estimated (*r₀*, *r₁*, *H*). This gives an expanded uncertainty of:

$$U_{vol} = \frac{2\pi}{3}\sqrt{(\Delta x^2 + (0.02)^2)[(r_0 r_1)^2 + (r_0 H)^2 + (r_1 H)^2]}$$

While the 5 cm voxel size was selected for the main analysis of tree geometry, the following tables provide the same estimates produced for both 10 cm and 15 cm voxels. This provides an evaluation of the influence of fire model grid resolution when using a voxelized representation for tree geometry.

Table F 2: Tree dimensions determined using a 10 cm voxel size, including combined expanded (k=2) uncertainties, representing a 95 % confidence interval.

Tree	Height (m)	Major Crown Radius (m)	Minor Crown Radius (m)	Crown Volume (m^3)
1	3.30 ± 0.20	1.21 ± 0.20	1.19 ± 0.20	6.54 ± 1.22
2	3.60 ± 0.20	1.13 ± 0.20	1.07 ± 0.20	5.73 ± 1.19
3	4.20 ± 0.20	1.46 ± 0.20	1.34 ± 0.20	9.86 ± 1.75
4	4.00 ± 0.20	1.22 ± 0.20	1.09 ± 0.20	6.92 ± 1.34
5	5.90 ± 0.20	1.56 ± 0.20	1.43 ± 0.20	17.30 ± 2.59
6	5.70 ± 0.20	1.49 ± 0.20	1.42 ± 0.20	15.23 ± 2.49

Table F 3: Tree dimensions determined using a 15 cm voxel size, including combined expanded (k=2) uncertainties, representing a 95 % confidence interval.

Tree	Height (m)	Major Crown Radius (m)	Minor Crown Radius (m)	Crown Volume (m^3)
1	3.30 ± 0.30	1.23 ± 0.30	1.22 ± 0.30	7.59 ± 1.87
2	3.60 ± 0.30	1.14 ± 0.30	1.10 ± 0.30	6.54 ± 1.81
3	4.20 ± 0.30	1.49 ± 0.30	1.35 ± 0.30	11.45 ± 2.63
4	4.05 ± 0.30	1.27 ± 0.30	1.13 ± 0.30	8.05 ± 2.11
5	5.85 ± 0.30	1.58 ± 0.30	1.48 ± 0.30	19.80 ± 3.96
6	5.70 ± 0.30	1.53 ± 0.30	1.47 ± 0.30	17.73 ± 3.81